npj | metamaterials

Article

https://doi.org/10.1038/s44455-026-00026-9

Machine learning-based mechanics of TPMS architected materials driven by unit-cell geometric features

Dimitrios C. Rodopoulos[1,4], **Georgios Mermigkis**[2,4], **Panagiotis Hadjidoukas**[2] & **Nikolaos Karathanasopoulos**[1,3] ✉

Architected materials have transformed engineering practice, enabling unprecedented control over effective thermal and mechanical properties. While inner design acts as a lever for the effective performance, deriving structure-property relations remains a major challenge, with an ever-increasing need for physics-motivated, wide-applicability models. This contribution elaborates a machine learning framework for the prediction of the effective mechanical and thermal properties directly from the unit-cell geometry. The formulation identifies and leverages a set of fundamental geometric features to accurately predict the Young's and Shear modulus, Yield strength, and Thermal conductivity of architected TPMS materials based solely on their unit-cell's Computer-Aided-Design (CAD) architecture. The resulting hypermodel provides high-accuracy predictions and the foundation for inner design explainability analysis, facilitating the identification of the most influential features. Topological descriptors that favour shear over uniaxial stiffness or yield strength are identified. Notably, a minimal set of three features, providing compactness, inner surface area, and shape variance information suffices to predict the effective TPMS mechanics within a 5% accuracy threshold. The results benchmark novel, physics-motivated, and interpretable modelling pathways, guiding material design and discovery.

Advances in the manufacturing of architected materials with intricate inner structures have ushered in a new era of engineering design and analysis[1–4]. Architected materials, also known as metamaterials, derive their effective properties primarily through their internal structure rather than their chemical composition[5–7]. For a given base alloy, the effective metamaterial performance can be substantially tuned through the appropriate selection of the underlying topology[8,9]. This enables the design of lightweight high-specific-strength materials with extraordinary functionalities[10], finding applications in the mechanical[11], aerospace[12], automotive, and blast protection sectors, to name a few.

Until now a wide range of unit-cell metamaterial architectures have been developed[7,13], several of them inspired by nature[14–16]. Diverse strut-based architectures have been developed[17,18], following hierarchical and biomimetic patterns[19,20]. Optimizing their pattern[21,22] has allowed for ultra-lightweight design spaces to be probed, concurrently controlling the effective mechanics[22–25]. In addition to strut-based designs, sheet-based TPMS architectures have received substantial attention because of their superior specific strength[18,26–29]. Their zero mean curvature architecture supports the minimization of stress concentrations, rendering them particularly favourable for structural and heat transfer applications[30–33]. Since Schoen's pioneering study of the gyroid (G) lattice in the early 1970s[34], more than hundred TPMS architectures have been identified[26]. The most widely used include Primitive, Gyroid, I-graph-Wrapped Package (IWP), and Diamond topologies. Several patterns are inspired by natural structures, such as the exoskeletons of insects (butterfly, beetle)[35]. Each TPMS configuration has unique stiffness, strength, and energy absorption characteristics, covering a broad spectrum of effective mechanical properties[36–38].

Given the vast design space of metamaterial architectures, computational methods have become essential for evaluating and optimizing their performance. Several strategies have been proposed to reduce the associated computational cost, including reduced database schemes[39], surrogate modeling, task parallelization[40], and spectral decomposition methods[41]. Recent advances in neural networks and deep learning have introduced new opportunities in material science and engineering, particularly for

---

[1]Department of Mechanical Engineering, New York University AD, Abu Dhabi, UAE. [2]Department of Computer Engineering and Informatics, University of Patras, Patras, Greece. [3]Department of Mechanical and Aerospace Engineering, New York University, Tandon School of Engineering, Brooklyn, NY, USA. [4]These authors contributed equally: Dimitrios C. Rodopoulos, Georgios Mermigkis. ✉e-mail: n.karathanasopoulos@nyu.edu

accelerating the design and property prediction of architected materials[42,43]. Convolutional neural networks (CNNs) have been widely adopted for predicting the mechanical responses of composites and architected structures[44]. CNN-based surrogate models have demonstrated strong potential for topology optimization in TPMS architectures, such as Schoen's Gyroid[34]. Furthermore, 2D CNNs have been developed for predicting the effective thermal conductivity directly from microstructural cross-sections, offering practical advantages over 3D reconstructions[45]. Beyond purely data-driven formulations, physics-informed neural networks and deep operator learning frameworks have simplified the modeling of multi-phase architected materials and complex mechanical responses[43,46].

In systems where dendrogram-type relations among input parameters can be identified, graph-based models have been favored. Graph Neural Network (GNN) and Graph Convolutional Network (GCN) architectures exhibit exceptional modeling capabilities for a wide range of physical and chemical processes[47]. Variational GCNs scale linearly with the number of graph edges, learning features through connectivity matrices. Based on GCNs, autoencoders that encapsulate the mechanical properties of lattice structures that associate structural properties with lattice architectures have been developed. Modified crystal graph CNN models have accurately described the structure-property relations for shell-lattices, leveraging graph representations to enable the design and discovery of new materials with exceptional mechanical and thermal properties[47]. Through finite element simulations on more than 40,000 microstructural configurations, comprehensive stiffness and heat conductivity tensors have been established, demonstrating the scalability of graph-based approaches. Conditional generative adversarial networks (CGAN) have demonstrated accurate and robust predictions of fundamental mechanical properties of Voronoi-type metamaterials, including the effective Young's modulus and Poisson's ratio[48].

The data representation strategy directly affects the performance and accuracy limits of a given modeling architecture. Different representations have been used depending on the application of interest. In modeling molecular structures, text strings[49] and fingerprint vectors[50] have been widely used, encoding lattice architectures into compact descriptors. Furthermore, 8-bit geometric descriptor modeling approaches[51] have been proposed to create lattice patterns, often combined with long-short memory architectures. Among the diverse data representation approaches, pseudo-randomized strut geometries have been encoded as binary data (0,1) that distinguish void from solid regions and train CNN models to predict the complete stress-strain response[42]. Moreover, 3D, nodal-scale representation of the topological space has been shown effective in the compact storage of structural design information, which can be effectively processed through transpose CNN operations for the concurrent prediction of a wide range of effective properties[43]. Mixed approaches combining string-type and image-based information have also been presented. Three canonical categories have emerged for intelligent metamaterials applications: wave-based neural networks, mathematical operations, and logic operations. These categories directly execute computation, detection, and inference tasks in physical space[52].

Despite the substantial progress in data-driven analysis and design of architected materials, generalizable machine-learning formulations that operate directly at the unit-cell geometry level remain scarce. Most existing approaches rely on deep-learning architectures-typically CNNs or graph-based networks-that are either topology-specific, require high-dimensional voxel or image representations, or act as black boxes with limited interpretability. As a result, they offer little insight into why particular TPMS architectures exhibit superior stiffness, shear resistance, yield strength, or thermal conductivity. Consequently, a physics- and data-based understanding of which geometric attributes fundamentally govern distinct mechanical and thermal responses has yet to be established, and the minimal set of descriptors required to capture these relations remains unknown. Moreover, predictive frameworks capable of simultaneously addressing elastic, plastic limits, and thermal properties using only CAD-level information, without reliance on topology-specific training or expensive preprocessing, are currently lacking.

The present work addresses these limitations by introducing a feature-based, interpretable machine-learning framework that links TPMS unit-cell CAD geometry to effective elastoplastic and thermal performance through a compact set of physically meaningful descriptors. Leveraging fundamental geometric features-quantifying compactness, surface area, inertia, and spatial heterogeneity-the proposed formulation enables accurate prediction of Young's modulus, Shear modulus, Yield strength, and Thermal conductivity across a diverse set of sheet-based TPMS architectures. Crucially, the framework supports systematic explainability analysis, revealing how different geometric characteristics selectively control uniaxial, shear, plastic, and conductive responses, and establishing clear feature-importance hierarchies. Beyond predictive accuracy, the study identifies a minimal, topology-agnostic descriptor set sufficient to capture the full performance space within a narrow error margin, thereby advancing physics-motivated understanding, reducing model complexity, and providing a scalable pathway for rational design and discovery of architected materials directly from CAD data.

Results

Feature engineering of architected sheet-based TPMS materials

The unit-cell topology of architected materials is defined by a set of geometric features that uniquely characterize its architecture. For the construction of the relevant database, diverse TPMS topologies are considered. In particular, nine TPMS architectures, including Gyroid (GY), I-graph-wrapped Package (IWP), Schwartz Primitive (SCP), Fischer-Koch (FKS), Schwartz Diamond (SCD), Lidinoid (LD), Split-P (SLP), I2-Y (I2Y) and Schoen's F-RD (FRD) are analyzed, their level set description summarized in Table 3 (Section 4.1). The different unit-cell configurations are illustrated in Fig. 1a.

For each TPMS topology, a set of features is computed, including intuitive design features, such as: the unit-cell volume fraction V_f (Eq. (5)), that is the material content within a given unit cell volume, the effective normalized surface area A_n (Eq. (6)), defined as the total area of the inner topological pathways, normalized by the area of the unit-cell cube; and the compactness C (Eq. (7)), which measures the surface area of the material phase relative to that of a solid sphere of equal volume.

Additional features include the directional effective moments of inertia I_{11}, I_{22}, I_{12}, characterizing the average resistance of the architected material to curvature-inducing loads (Eq. (8)). For their computation, a voxel representation of the unit-cell topology is elaborated, averaging the moments of inertia computed along several cross-sections of the unit-cell, as schematically depicted in Fig. 1d. The moments are normalized with respect to the reference moment of inertia value of the solid unit-cell cube for dimensional analysis consistency purposes.

Furthermore, four additional geometric features derived from point-wise comparisons of the unit-cell architecture with the surface of a sphere having the same volume fraction with the one considered are elaborated (see Section 4.1). In particular, a cloud of N_S points $G \circ S^2 = \left\{ \boldsymbol{\xi}^i \in S^2(\rho), i = 1, 2, \ldots, N_S \right\}$ distributed on a spherical surface $S^2(\rho)$ is mapped to the TPMS surface M, forming the following collection of point pairs: $f(G \circ S^2, G \circ M) = \left\{ (\boldsymbol{\xi}, \mathbf{x}) | \boldsymbol{\xi} \in G \circ S^2(\rho), \mathbf{x} \in G \circ M, \mathbf{R}(\mathbf{x}; \boldsymbol{\xi}) = \mathbf{0} \right\}$. The set of point pairs allows for the computation of an average distance $\bar{D}$, a variance $\mathrm{Var}(D)$, as well as a minimum $\min(D)$ and maximum distance $\max(D)$, among the unit-cell topology and the points of the sphere (Eq. (16)).

A detailed overview of the geometric features is provided in Fig. 1b–d. In particular, Fig. 1b presents the evolution of V_f for an IWP unit cell, along with examples of different compactness values relative to the limiting value $C = 1$ of a sphere $B(\rho^*)$. Moreover, a graphical example of the effective surface area A_n is provided, defining the associated surface boundaries. Figure 1c presents the shape-distance features: a Primitive minimal surface is shown together with the point clouds $G(S^2(\rho))$ (blue) and $G(M)$, where the distances $d(\mathbf{x}^i; \boldsymbol{\xi}^i)$ are defined, as well as the description of the associated metrics $\bar{D}$, $\mathrm{Var}(D)$, $D_{\min}$, $D_{\max}$. Figure 1d illustrates the pixel-based calculation procedure of the inertia features I_{11}, I_{22}, I_{12}, according to[53]. For a given

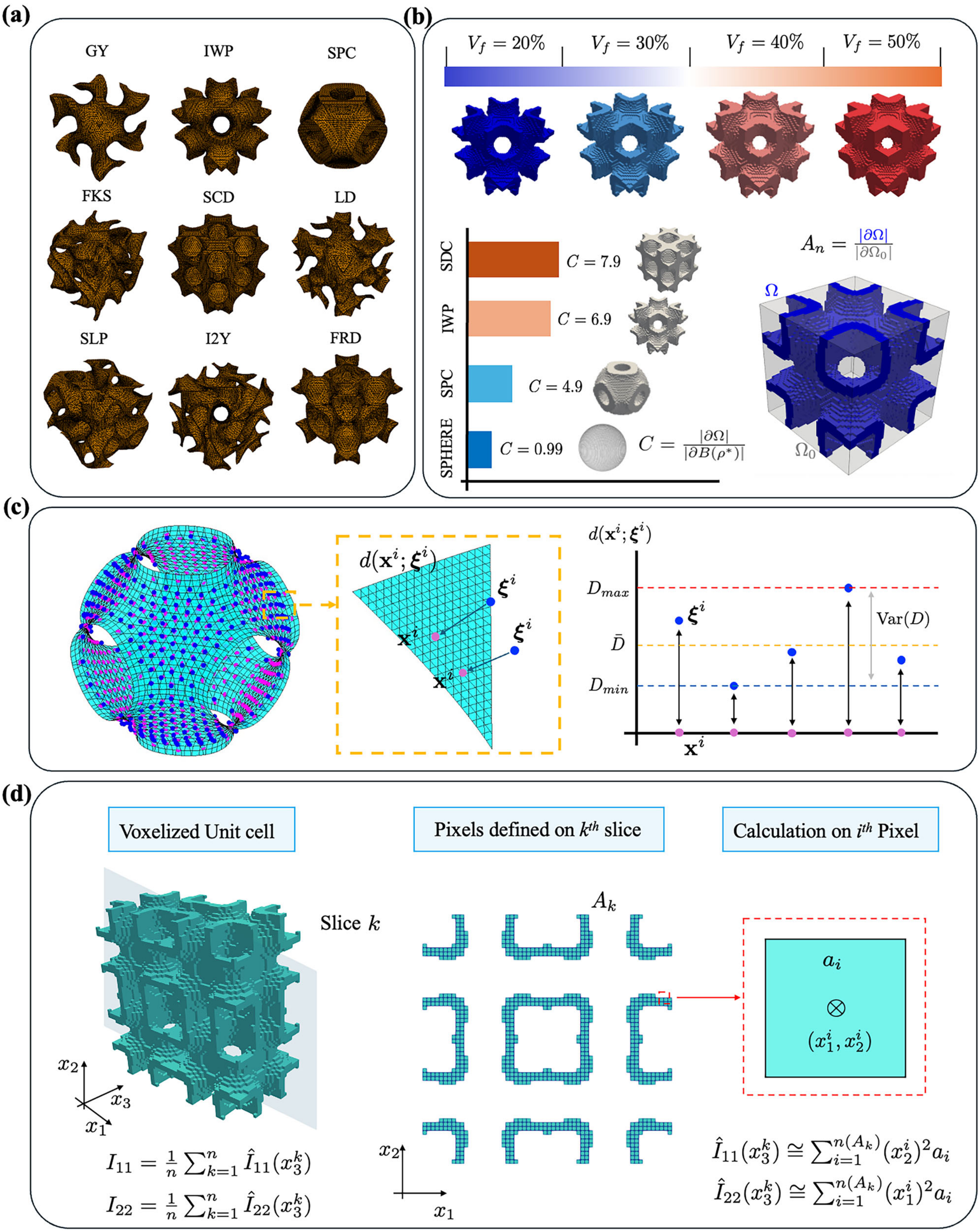

Fig. 1 | Overview of TPMS unit-cell topologies and geometric feature extraction. **a** Unit cells of TPMS sheet-based architected materials, **b** Volume fraction V_f, compactness C and inner normalized surface area A_n. The compactness is the ratio of the material phase area to the area of a sphere $B(\rho^*)$ with equal volume, i.e $|\Omega| = |B(\rho^*)| = \frac{4}{3}\pi(\rho^*)^3$, **c** Description of the algorithm for the shape irregularity metrics: The blue points belong to the spherical surface, whereas the purple ones represent their maps to the corresponding TPMS, and, **d** the algorithm for the pixel-based calculation of inertia features.

TPMS unit cell, the inertia values are obtained averaging with respect to n slices along the x_3 direction, where, for each slice k, the corresponding inertia integrals are approximated using the corresponding set of pixels (Eq. (9)).

A detailed statistical assessment of the selected geometric features is presented in Fig. 2a, c-e, for the considered topology set (Fig. 1a). For the analysis, the prescribed volume fraction V_f values vary in the interval [0.2, 0.5] (Fig. 1b). The Pearson correlation map in Fig. 2a indicates weak correlations among most features, with the exception of those inherently correlated, attesting to the accuracy of the underlying computations. In particular, a unity colleration among the moments of inertia I_{11} and I_{22}, along the x_1 and x_2 axis is revealed, reflecting the centrosymmetry of most unit-cell designs. Moreover, the compactness C and effective area A_n metrics yield high correlation values, both of them being area-related metrics. Furthermore, the unit-cell moments of inertia are strongly correlated with the compactness C and effective area A_n metrics, a dependence that can be appreciated by the Steiner's parallel axis theorem, which includes area attributes from its very definition (Eq. (8)). All remaining features exhibit comparatively lower correlations, indicating a significant contribution to the overall geometric information available for the hypermodel creation.

The evolution of compactness C for each topology and for two representative volume fractions, $V_f = 0.26$ and $V_f = 0.42$ is provided in polar diagrams in Fig. 2a. Higher compactness values are recorded for the low-volume case ($V_f = 0.26$) consistent with the fact that materials with smaller V_f exhibit relatively larger internal surface areas within the unit cell. Significant compactness variations as a function of topology are recorded, with the volume fraction to modify the values, but not the overall distribution among the different unit-cell designs. For both volume fractions, I2Y, Fischer-Koch, and Lidinoid topologies yield the highest C values.

Probability density distributions of the distance metrics ($\bar{D}$, Var(D)) for all unit-cell designs are provided in Fig. 2c, summarized in the form of boxplots in Fig. 2d. The widest spread is observed for $D_{\min}$ (red-colored filled distribution and boxplot in Fig. 2c) with a mean value in the order of 0.003 and a considerable variance. In contrast, the maximum distance $D_{\max}$ (salmon color in Fig. 2c) presents the lowest variance variance. The mean point-wise distance $\bar{D}$ has a value of 0.153, while the variance Var(D) a value of 0.018, being nearly an order of magnitude lower. It should be noted that the distance metrics are insensitive to the volume fraction V_f, their value controlled by the topological architecture. Indicatively, Gyroid unit-cell designs have a mean distance $\bar{D}$ of 0.09, while IWP architectures have almost twice the value, namely 0.172 (Fig. 2c)).

The inner surface area A_n distribution (Fig. 2e) overall follows the pattern recorded for the compactness C metric (Fig. 2b), with I2Y, Fischer-Koch, and Gyroid, SPC architectures to yield the highest ($A_n = 3.92$, $A_n = 3.71$) and lowest ($A_n = 2.28$, $A_n = 1.76$) values, respectively. However, while the topological classification closely matches that recorded in the compactness C metric, the relative scaling among the topologies well differs. Interestingly, unit-cell architectures with low surface area A_n metrics are those with the highest inertia $\widehat{I}_{11}$ values, with SCP, Gyroid and IWP architectures to populate the upper part of Fig. 2f. Moreover, the relative density V_f dependence of $\widehat{I}_{11}$ is non-linear, with certain architectures to achieve high values already at moderate densities, with the actual value to be highly topology dependent.

Mechanical and thermal performance space

Comprehensive insights into the mechanical and thermal conductivity response space are provided in Fig. 3. The effective Young's modulus $\widehat{E}$, thermal conductivity $\widehat{\kappa}$, shear modulus $\widehat{G}$, and uniaxial loading yield stress $\widehat{\sigma}_y$ are evaluated for the different sheet-based TPMS architectures of Fig. 1, for relative density values as low as 20% and up to 50% through voxel-based finite element analysis (Section 4.4). Dedicated voxelization convergence analysis and validation comparisons with existing studies are provided in the Supplementary Material (S1) for completeness purposes. In the sequel, the effective performance metrics are normalized by the base material properties of solid aluminum: the Young's and shear moduli are normalized by $E_{\text{ref}} = 69$ GPa, the effective thermal conductivity by $\kappa_{\text{ref}} = 237$ W/mK, while the yield stress by the yield limit of aluminum ($\sigma_y = 250$ MPa).

The kernel density estimation (KDE) plots in Fig. 3a illustrate the variation of the average value of each effective property with respect to the Compactness and Inner Surface area metrics (A_n, C), across the entire geometric features space (gray background). A broad Young's modulus distribution is recorded, with the highest average value observed for the Schoen's F-RD topology (FRD, $\bar{\widehat{E}} = 0.21$), and the lowest for Primitive SPC architectures, for which nearly half average values are computed ($\bar{\widehat{E}} = 0.11$). Notably, high mean Young's moduli are recorded for IWP ($\bar{\widehat{E}} = 0.18$), FKS ($\bar{\widehat{E}} = 0.17$), and SLP ($\bar{\widehat{E}} = 0.17$) TPMS architectures, classifying them among the stiffest -on average- unit-cell patterns. The corresponding mean effective thermal conductivity distributions demonstrate a narrower spread (Fig. 3b). The lowest thermal conductivities are recorded for Lidinoid architectures ($\bar{\widehat{\kappa}} = 0.21$), with Primitive SPC designs to furnish the highest, on-average, mean value ($\bar{\widehat{\kappa}} = 0.25$, SPC) for the lowest combination of A_n, C.

The shear modulus distribution well differs from that recorded for the Young's modulus and thermal conductivity values (Fig. 3c). Primitive SPC designs appear to be the shear stiffest patterns ($\bar{\widehat{G}} = 0.06$), despite their low Young's modulus. Interestingly, SCD unit-cell architectures record the lowest mean shear modulus values, despite their moderate Young's modulus and thermal conductivity (Fig. 3a, b). The distribution of the average uniaxial yield stresses (Fig. 3d) better compare with that of the Young's modulus. However, their mean values indicate smoother topological dependencies, with the normalized bounds ranging between $\bar{\sigma}_y = 0.11$ and $\bar{\sigma}_y = 0.15$ for the Lidinoid and Schoen's F-RD unit-cell architectures.

Further statistical information is provided in the violin plots of Fig. 3e–h. The plots provide insights not only into the comparative performance for each unit-cell design, but also into the property distribution of a given architecture, upon varying volume fractions V_f (vertical axis). In particular, the width of each violin distribution represents the probability density of observing a particular property value.

The Young's modulus distributions of Fig. 3e indicate a wide range of values, as low as $\widehat{E} = 4$ and up to $\widehat{E} = 35$ MPa, with the Schoen's F-RD architecture populating the highest moduli space and Primitive SPC the lowest. Across all unit-cell designs, the lower part of the corresponding violins are wider, indicating that the probability density distributions with lower $\widehat{E}$ values are more frequent for the same V_f space. The representative uniaxial loading von Mises (σ_{VM}) stress distributions (Fig. 3e, Section 2.2) highlight the strong differences in the internally highly stressed regions for IWP, SPC, and SCD unit-cell designs with a common V_f value of 0.30 under the same magnitude of macroscopic stress.

The distribution of effective thermal conductivities $\widehat{\kappa}$ is smoother, with comparable violin column heights across most unit-cell designs, as well as relatively uniform probability density distributions denoted by the low variation of the violin widths (Fig. 3f). Primitive SPC and FRD furnish the highest average $\widehat{\kappa}$ values, their distribution ranging between $\widehat{\kappa} = 0.14 - 0.36$ and $\widehat{\kappa} = 0.15 - 0.38$ $W/(m \cdot K)$, respectively. Contour plots of the temperature gradient magnitude $|\nabla\ \theta|$ illustrate distinct thermal flux pathways among the IWP, Primitive SPC, and SCD unit-cell designs, with the overall distributions exhibiting similarities with the von Mises stress distributions of Fig. 3e.

Contrary to the rather smooth distribution of thermal conductivities, shear moduli reveal significant unit-cell dependencies (Fig. 3g). Primitive SPC and Schoen's F-RD yield shear moduli values that range between $\widehat{G} = 0.03$ to 0.10 and $\widehat{G} = 0.025$ to 0.09, respectively, with Primitive architectures exhibiting a more uniform density distribution across the violin height. Lidinoid unit cells are comparatively shear shofter, their upper modulus range restraining below 6.939043 MPa. The associated shear von Mises σ_{VM} contour plots highlight the utterly different inner unit-cell

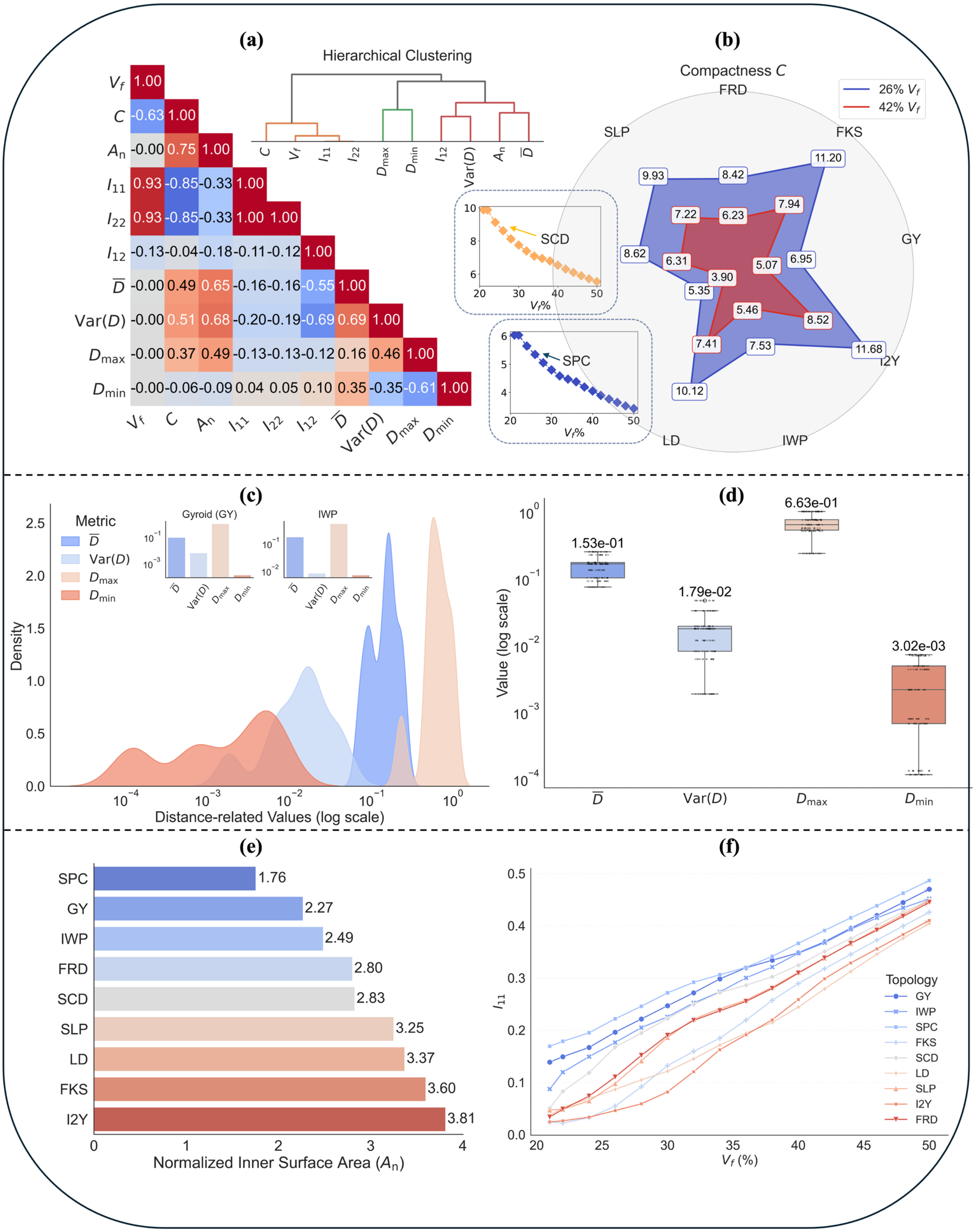

Fig. 2 | Geometric feature analysis of TPMS sheet networks. a Pearson correlation matrix between geometric descriptors with hierarchical clustering dendrogram. **b** Compactness C comparison across topologies for 26% and 42% V_f. **c** Probability density distributions of distance-related metrics on a logarithmic scale. **d** Statistical distributions of distance metrics (boxplots shown on log scale). **e** Average normalized inner surface area A_n across topologies. **f** Evolution of the moment of inertia components I_{11}, I_{22}, and I_{12} with volume fraction for each topology.

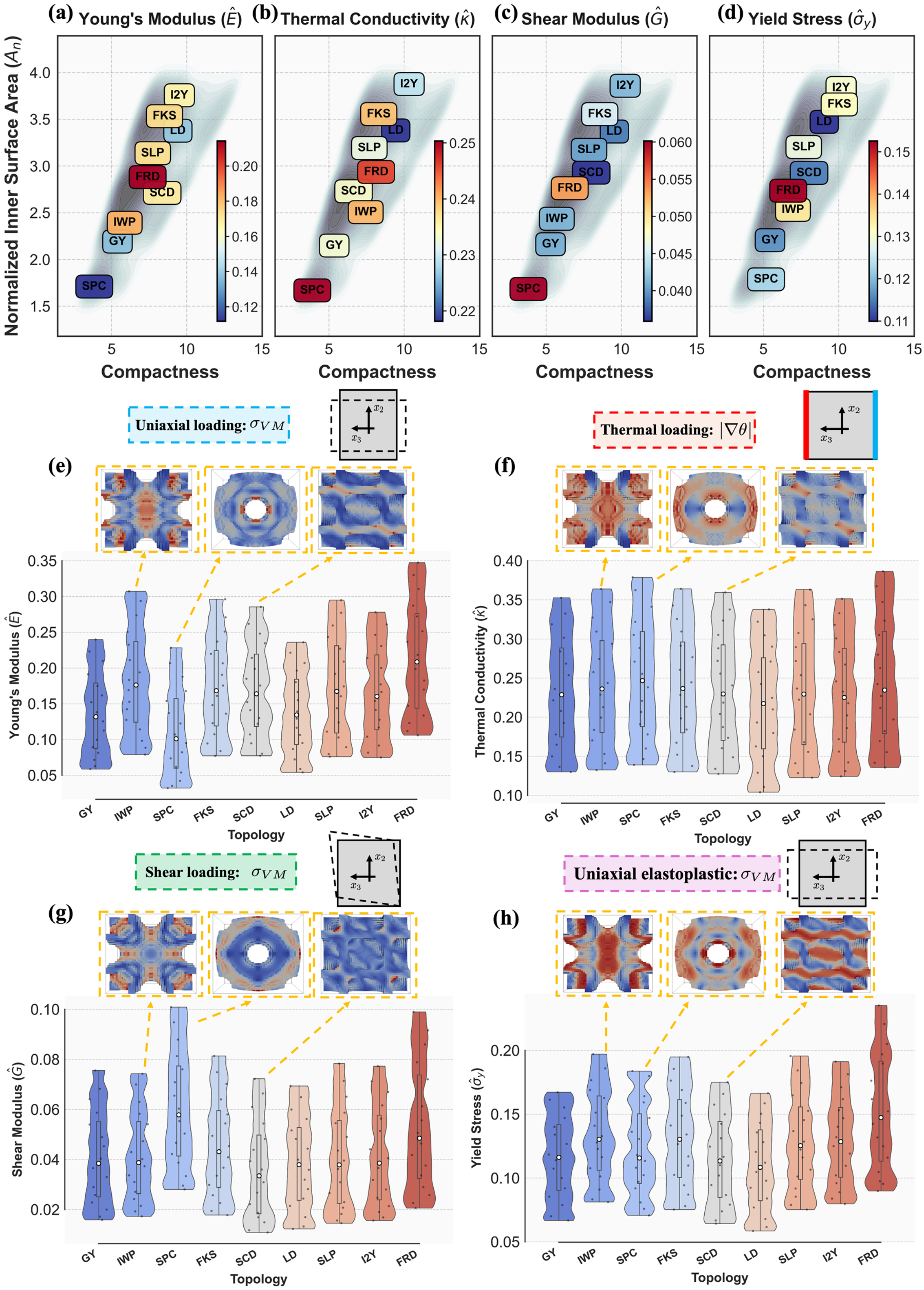

Fig. 3 | Effective mechanical properties of TPMS sheet topologies. a–d Density relationships between normalized mechanical and thermal properties and the geometric descriptors compactness and normalized inner surface area A_n. **e–h** Violin distributions of the effective properties across topologies, aggregating all investigated volume fractions, with representative von Mises stress contour plots under (**e**) uniaxial elastic, (**f**) thermal, (**g**) shear, and (**h**) uniaxial elastoplastic loading.

material regions primarily loaded compared to the tensile or thermal loading cases (Figs. 3g vs e, f).

The violin plots of the effective yield stresses (Fig. 3h) reveal overall comparable topology dependencies with those recorded for the Young's modulus (Fig. 3e). FRD TPMS architectures define the upper performance bounds, achieving the highest mean value of $\widehat{\sigma}_y = 0.153$. In contrast, Lidinoid unit-cell architectures exhibit the lowest mean yield stress, with $\widehat{\sigma}_y \approx 0.11$ across the investigated volume-fraction range. The accompanying yield stress contour plots reveal spatial patterns that are analogous to the von Mises stress distributions observed under uniaxial elastic loading (Fig. 3e), highlighting the strong correlation between stiffness and yield-dominated response.

Explainability analysis

Predictive modeling of the effective mechanical and thermal properties of TPMS-based architected materials was carried out using Random Forest (RF) and Extreme Gradient Boosting (XGBoost) regressors. Deep Learning (DL) modeling has been as well evaluated, relevant insights provided in the Supplementary Material (S5) for completeness purposes. The input feature vector **X** consists of the geometric descriptors defined in Section 4.2, excluding I_{22}, as it is fully correlated with I_{11}(Fig. 2):

$$\mathbf{X} = (V_f,\, C,\, A_n,\, I_{11},\, I_{12},\, \bar{D},\, \mathrm{Var}(D),\, D_{\max},\, D_{\min}) \in (\mathbb{R}^{+})^{9} \tag{1}$$

The regression targets are the effective Young's modulus $\widehat{E}$, thermal conductivity $\widehat{\kappa}$, shear modulus $\widehat{G}$, and yield stress $\widehat{\sigma}_y$:

$$\mathbf{Y} = (\widehat{E},\, \widehat{\kappa},\, \widehat{G},\, \widehat{\sigma}_y) \in (\mathbb{R}^{+})^{4} \tag{2}$$

The models were trained employing stratified train-test splitting, elaborated in Section 4.2, while 5-fold cross validation was as-well performed. A schematic workflow of the machine learning training process is provided in Fig. 6. For the analyzed performance space, consisting of a total of 144 samples, RF and XGBoost models exhibited an overall higher robustness in the modeling of the effective performance compared to DL models (see Supplementary Material S5), consistently achieving high coefficients of determination ($R^2 > 94\%$) across all predicted properties. In the sequel, RF and XGBoost models are employed as the basis for feature importance and explainability analysis tasks. In particular, model interpretability is assessed using built-in feature importance metrics and SHapley Additive exPlanations (SHAP)[54], which quantify the contribution of each feature to individual predictions. More information on SHAP analysis and feature interactions is provided in Section 4.3.

Entire feature set X. In the SHAP feature importance rankings of Fig. 4(a–d) developed based on the complete set of input features **X** (Eq. (1)), V_f dominates the prediction of all performance metrics, including the Young's modulus $\widehat{E}$, thermal conductivity $\widehat{\kappa}$, and yield stress $\widehat{\sigma}_y$, except for the shear modulus $\widehat{G}$. For $\widehat{G}$, the moment of inertia I_{11} is comparable in significance to the volume fraction. For the Young's modulus $\widehat{E}$ and the yield stress $\widehat{\sigma}_y$, the mean absolute V_fSHAP values are more than three and six times higher than the average surface-to-sphere distance $\bar{D}$, which ranks second. Interestingly, $\bar{D}$ is comparatively more important for the Young's modulus $\widehat{E}$, than for $\widehat{\sigma}_y$. The moment of inertia I_{11} and compactness C populate the third and fourth positions of importance for $\widehat{E}$, which are otherwise occupied by the maximum distance D_{max} and coupling moment of inertia I_{12} for the yield stress metric $\widehat{\sigma}_y$.

The contributions of I_{11}, D_{max} and $\bar{D}$ to the effective thermal conductivity performance $\widehat{\kappa}$ are highlighted in the mean SHAP values of Fig. 4b, which appear as the next most important features after V_f in the corresponding importance metrics. However, for the shear modulus $\widehat{G}$, the effective moment of inertia I_{11} is approximately 60% as important as the volume fraction. It is the only response metric in which the dominance of V_f is not as prominent. In the set of the most influential features for shear $\widehat{G}$ performance, the maximum distance $D_{\max}$ and unit-cell compactness C occupy the third and fourth most important positions, respectively.

Higher volume fraction values monotonically increase all effective metrics, as schematically illustrated in the violin density diagrams of Fig. 5. The same monotonic dependence is recorded for the mean distance $\bar{D}$, primarily affecting the Young's modulus $\widehat{E}$ and yield stress $\widehat{\sigma}_y$ (Fig. 5a, d). An analogous nonlinear increasing property dependence is observed for I_{11}, as of its high correlation with V_f.

Feature set X-{V_f}. Excluding the volume fraction V_f from the list of features and retraining the ML model reveals a dominance for the moment of inertia I_{11}, which ranks first for all four performance metrics (Figs. 4(e–h)). For the effective Young's modulus $\widehat{E}$ and yield stress $\widehat{\sigma}_y$, surface area and distance metrics appear on the 2nk to 4rth ranking positions, with A_n, $\bar{D}$ and $\mathrm{Var}(D)$, $\bar{D}$ to populate the second and third place, respectively. For $\widehat{\kappa}$, the effective surface area A_n and distance variance $\mathrm{Var}(D)$ arise as the 2nd and 3rd most important features, while for the shear modulus $\widehat{G}$, their order is inverted, with the distance variance $\mathrm{Var}(D)$ being more important than the effective surface area A_n. It should be highlighted that the moment of inertia I_{11} is highly correlated with the volume fraction V_f, the corresponding Pearson's correlation metric exceeding 90% in Fig. 2.

Feature set X-{V_f, I_{11}}. Upon the omission of both V_f and I_{11} from the set of characteristics (Fig. 4(i–l)), the strong correlation of compactness C with I_{11} (85%, Fig. 2a), and the implicit calibration of compactness C to the volume fraction (see Eq. (7)) drives its importance to the leading position. The Young's modulus $\widehat{E}$, and yield stress $\widehat{\sigma}_y$ continue to place the surface area A_n and $\mathrm{Var}(D)$ as the two most important features after C. Accordingly, the surface area A_n and distance variance $\mathrm{Var}(D)$ continue being the most important metrics for the effective thermal conductivity $\widehat{\kappa}$ and shear modulus $\widehat{G}$ (Fig. 4k), consistent with the observations made for the $\mathbf{X}$-$\{V_f\}$ feature set case (Fig. 4g). It should be underlined that both surface-related (A_n) and spatial heterogeneity ($\mathrm{Var}(D)$) descriptors are strongly correlated with the mean distance $\bar{D}$ metric (Fig. 2a), an observation justifying the comparatively lower importance placement of $\bar{D}$ in the corresponding ranking.

The violin density diagrams of Fig. 5(e–h) verify the above-elaborated feature importance metrics in the form of distribution plots. It is noteworthy that compactness C follows a highly comparable distribution for all effective performance attributes, the distribution differences concentrated in the second and third most important feature, namely the surface area A_n and distance variance $\mathrm{Var}(D)$. While surface area is visibly more informative than distance variance $\mathrm{Var}(D)$ for the Young's modulus $\widehat{E}$ and thermal conductivity $\widehat{\kappa}$, this is not case for the shear response ($\widehat{G}$) and yield limit $\widehat{\sigma}_y$ (Fig. 5g, h). Increased distance variances $\mathrm{Var}(D)$ lead to higher $\widehat{G}$ and $\widehat{\sigma}_y$ values, their positive SHAP distribution density and range being directly comparable or higher of that recorded for the surface area A_n.

The remaining features (I_{12}, $\bar{D}$, $D_{\max}$, $D_{\min}$) exhibit substantially lower contributions and act as tertiary descriptors of fine-scale geometric variation. Overall, the three-stage SHAP analysis establishes a clear hierarchy of geometric influence: (i) V_f controls global scaling of all properties, (ii) I_{11} captures dominant inner design structural effects, and (iii) compactness C, surface-area A_n and topology heterogeneity $\mathrm{Var}(D)$ descriptors encode the intrinsic morphological contribution to mechanical and thermal performance.

Beyond individual feature importance, interaction analysis reveals synergistic effects among geometric descriptors (Table 1). When volume fraction and I_{11} are excluded, compactness C becomes the dominant feature, showing significant interactions with I_{12} across multiple properties (correlations 0.45–0.83). This coupling is most pronounced for the shear modulus (0.83), suggesting that shape irregularity and biaxial moment distribution critically contribute to the shear response in the absence of volumetric information. For the yield stress, C demonstrates moderate interactions with I_{12} (0.52) and mean distance $\bar{D}$ (0.36), while the distance variance $\mathrm{Var}(D)$

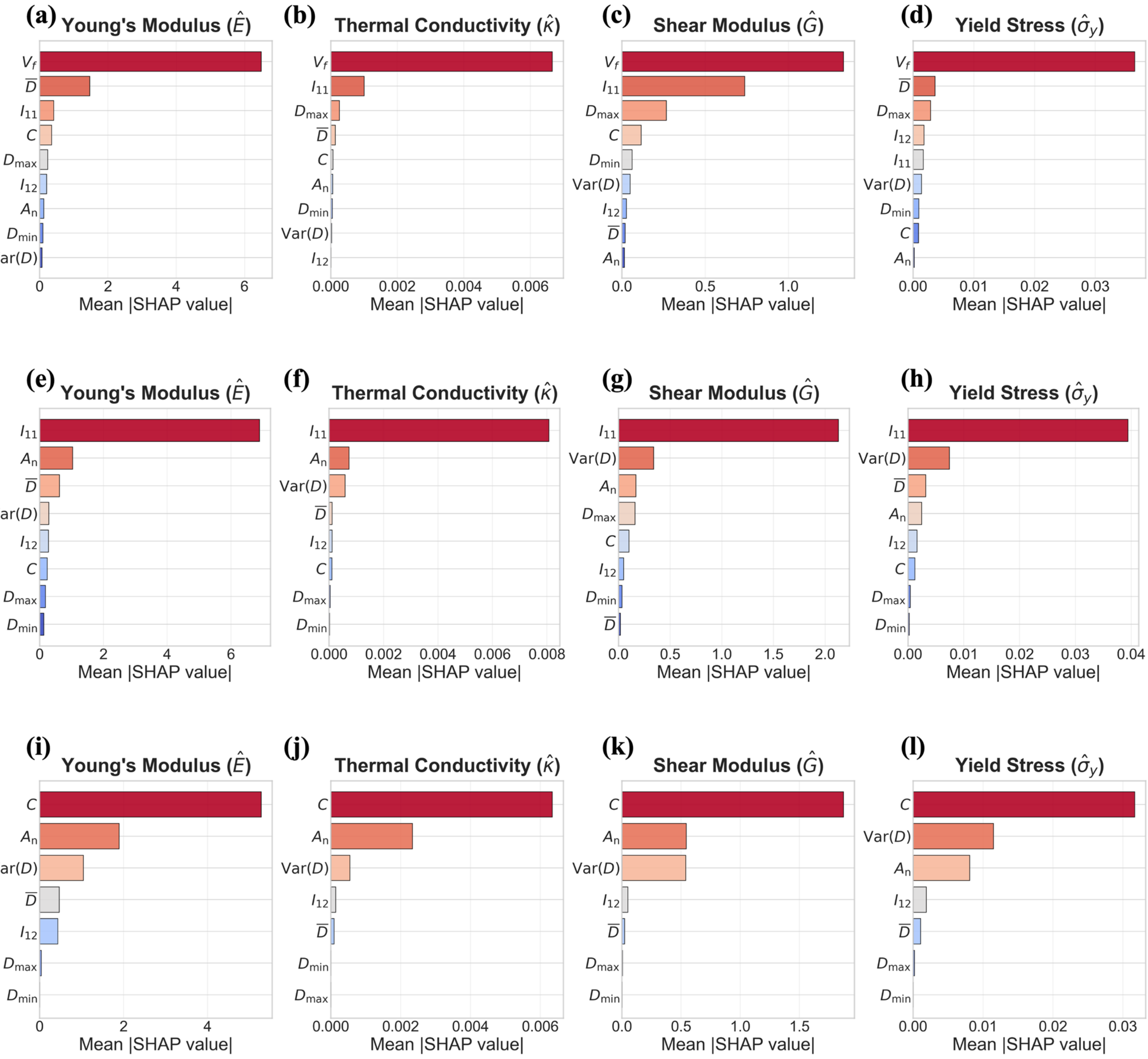

Fig. 4 | SHAP analysis of XGBoost feature importance with progressive feature exclusion. a–d SHAP feature importance with full feature set including volume fraction V_f. **e–h** SHAP feature importance excluding volume fraction V_f. **i–l** SHAP feature importance excluding both V_f and principal moment of inertia I_{11} to reveal intrinsic contributions of remaining geometric descriptors.

shows strong coupling with $\bar{D}$ (0.46), indicating that void spacing distribution patterns govern plastic deformation onset. The shift from V_f-I_{11} dominated interactions to C-I_{12} coupling upon feature removal highlights the hierarchical nature of geometric influence on mechanical response.

Minimum Feature Set X_{min}-{V_f, I_{11},…,D_{min}}. A progressive feature elimination process was followed to reduce the set of input features while preserving those informative enough for predicting the effective mechanical and thermal properties. The process began by removing the metrics contributing least to the SHAP importance rankings (Figs. 4(i–l) and 5(e–h)). Removing the maximum and minimum unit-cell distances (D_{max}, D_{min}) and retraining the XGBoost model with the remaining five descriptors results in comparable predictive performance, with all coefficients of determination R^2 exceeding 0.96 across the target properties. Further excluding the mean distance $\bar{D}$ and the coupling moment of inertia I_{12} still preserves high predictive fidelity, with R^2 remaining above 0.95 for all targets. Ultimately, only three features-compactness C, normalized surface area A_n, and distance variance Var(D)-are sufficient to capture the full performance space, with all R^2 values above 0.95 (Fig. 7d in Section 4.3). Any additional reduction in the feature set leads to substantial drops in R^2, confirming that this minimal set contains the essential topological information for accurate property prediction. As further evidenced by the 5-fold cross-validation results in Table 2, the minimal feature set provides higher average R^2 values than the two intermediate feature-reduced configurations, highlighting its core predictive efficiency.

Minimum feature set estimates on scarce and extrapolated data. The performance of the minimum feature set $\mathbf{X}_{min} = \{C, A_n, Var(D)\}$ is subsequently evaluated on extreme modeling cases, namely on scarce data (a) and extrapolated data (b). In the scarce dataset case, a particularly critical case for machine learning modeling[55,56], the 144 initial samples are reduced to 117, a reduction of ~ 19%, randomly removing three (3) relative density datapoints per topology. Interestingly, XGBoost modeling achieves R^2 values above 94% for all performance metrics except for the yield stress ($R^2_{\sigma_y}$ =~ 92%), the relevant results summarized in the Supplementary Material (S3).

In the extrapolation testing case (b), a leave-one-topology-out (b-i) and a substantial out-of-volume-fraction-bounds (b-ii) scenario were tested. In

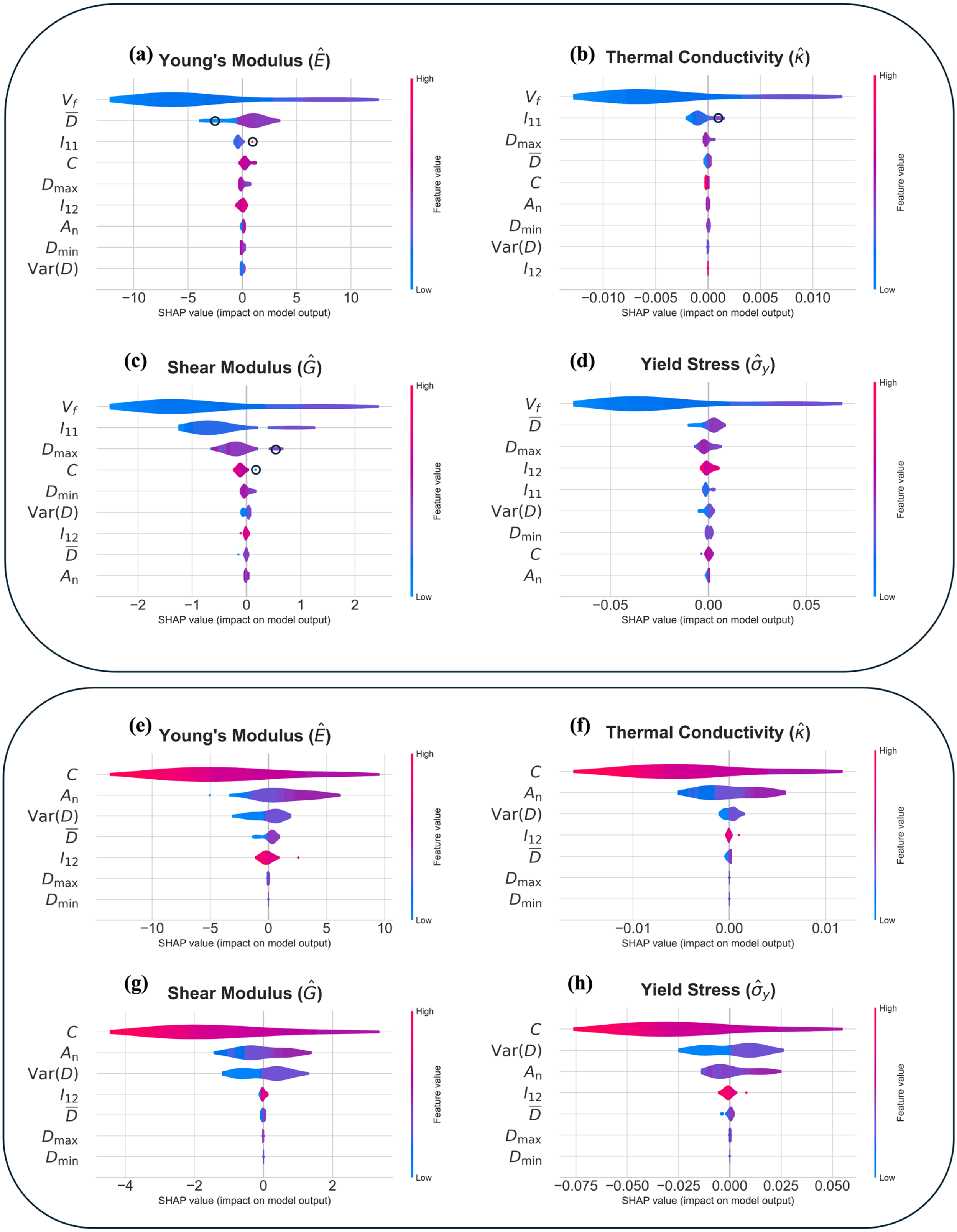

Fig. 5 | SHAP violin plots for mechanical and thermal properties. a–d Top box: Young's modulus $\widehat{E}$, thermal conductivity $\widehat{\kappa}$, shear modulus $\widehat{G}$, and yield stress $\widehat{\sigma}_y$ using the full feature set. **e–h** Bottom box: Corresponding SHAP distributions after exclusion of volume fraction V_f and principal moment of inertia I_{11}.

the first case (b-i), the Lidinoid (LD) topology has been completely removed from the training set and has been exclusively used for testing, training the model on the remaining TPMS topologies. As such, a completely blind test has been performed, practices at the limits or beyond the performance bounds of supervised learning methods[57,58]. Under this leave-one-topology-out testing setting, the model achieved an R^2 of 0.82 and 0.84 for the Young's modulus and yield stress, respectively, retaining R^2 scores above 94% for the effective thermal conductivity and shear modulus. In the second out-of-volume-fraction-bounds case, the model was trained in the 20–50% volume fraction range and tested in two separate ranges: in the

$[0.17-0.18-0.19, 0.51-0.52-0.53]$ for (b-ii-a), and in $[0.10-0.20]$ for (b-ii-b). In (b-ii-a), R^2 scores above 95% were obtained for all elastic properties, with the yield stress accuracy reduced to ~ 88%, while in the (b-ii-b) case, R^2 elastic property scores ranged in-between 85 and 95%, with the yield stress accuracy reducing to 73% (see Supplementary Material S2, S4). Considering the fact that the model is evaluated in blind spaces, not favorable to supervised learning, the results highlight the strong predictive performance of the identified minimal feature set $\mathbf{X}_{min}$ for sheet-based TPMS topologies.

Discussion

The results provide evidence that the effective mechanics of TPMS metamaterials are driven by a finite set of fundamental topological features[26], with substantially low dimensionality, well below the representation spaces arising from image-based convolutional feature extraction processes. Interestingly, a set of three fundamental features that encompasses compactness, inner surface area, and distance variance metrics is sufficient to accurately predict the elastoplastic and conductive performance of sheet-based TPMS architectures with remarkable accuracy, indicating that the dominant structure–property relations can be captured upon minimal, yet high-density, information.

This significantly reduces the computational cost of prediction and yields interpretable descriptors that directly link internal geometric characteristics to macroscopic response. From a design perspective, the identification of a fundamental set of CAD-accessible features enables rapid screening and inverse exploration of architected materials without the need for the development of dedicated, case-study-specific, finite element models. The resulting machine learning models can be directly integrated into design workflows for multi-objective optimization of mechanical and thermal performance, while remaining interpretable and computationally efficient.

Nevertheless, despite the significant number of TPMS unit-cell architectures and volume fractions considered for the development of the feature-property database, all designs fall within the class of sheet-based structures. Extending the framework to additional topological classes-such as strut-based, hybrid, graded, and stochastic architectures-would enable a level of generalization that remains largely infeasible for existing machine learning formulations, thereby supporting substantially broader applicability. Within this expanded design space, however, the incorporation of additional feature descriptors-such as connectivity-related metrics and material gradient information, among others-may be necessary to adequately capture the underlying structural complexity. Such an objective would require the development of sufficiently large and representative databases, overcoming fundamental bottlenecks inherent to machine learning modeling[55]. In turn, enhanced and extended models could integrate additional effective performance descriptors, including effective buckling limits[59], and dynamic transmissibility attributes, which have the potential to decisively expand the model's predictive deployment across a wide range of engineering applications.

Overall, feature-based, interpretable machine learning models provide a robust and data-efficient pathway for establishing inner structure–functional property relations of architected materials. By bridging CAD-level geometry with macroscopic performance through a compact set of physically meaningful descriptors, the elaborated framework lays the foundation for rational, explainable and scalable design of multifunctional architected materials.

Table 1 | SHAP feature interactions excluding the volume fraction V_f and principal moment of inertia I_{11} metrics

Target Property	Feature	Primary Interactions	Correlations
Young's Modulus	C	$D_{\max}$, I_{12}, $\bar{D}$	0.47, 0.45, 0.36
	A_n	I_{12}, Var(D), $\bar{D}$	0.59, 0.36, 0.22
	Var(D)	$D_{\min}$, A_n, C	0.41, 0.36, 0.25
Thermal Conductivity	C	I_{12}, $\bar{D}$, Var(D)	0.50, 0.36, 0.20
	A_n	Var(D), $\bar{D}$, I_{12}	0.37, 0.21, 0.12
	Var(D)	$\bar{D}$, A_n, C	0.41, 0.37, 0.20
Shear Modulus	C	I_{12}, $D_{\max}$, $\bar{D}$	0.83, 0.44, 0.33
	A_n	$D_{\max}$, Var(D), C	0.39, 0.26, 0.13
	Var(D)	$D_{\min}$, $\bar{D}$, C	0.61, 0.55, 0.32
Yield Stress	C	I_{12}, $\bar{D}$, Var(D)	0.52, 0.36, 0.35
	Var(D)	$\bar{D}$, C, I_{12}	0.46, 0.35, 0.16
	A_n	$\bar{D}$, $D_{\max}$, C	0.22, 0.16, 0.11

The top 3 features per target property are presented along with their strongest interaction partners, measured through SHAP correlation.

Methods

Triply periodic minimal surface-based metamaterials

The present study focuses on architected materials with topology that is based on Triply Periodic Minimal Surfaces (TPMS)[29,60]. TPMS represent a class of surfaces with zero mean curvature, i.e:

$$\begin{aligned} M_{TPMS} &= \left\{\mathbf{x}=(x_1,x_2,x_3)\in\mathbb{R}^3 \middle| \varphi(\mathbf{x})=t, H(\mathbf{x})=0\right\} \\ H(\mathbf{x}) &= \tfrac{1}{2}\nabla\cdot\left(\frac{\nabla\varphi(\mathbf{x})}{|\nabla\varphi(\mathbf{x})|}\right) \end{aligned} \tag{3}$$

Consider the unit cell $\Omega_0=[0,L]^3\in\mathbb{R}^3$, with $L=1$, forming a metamaterial structure V by repetitions in every direction of the space. Let Ω be the part of the unit cell Ω_0, that corresponds to the metamaterial with topology that can be characterized as a solid or sheet based network by the following definition:

$$\text{Sheet network}-\text{based unit cell}\ :\ \Omega=\{\mathbf{x}\in\Omega_0|-t\leq\varphi(\mathbf{x})\leq t\} \tag{4}$$

Table 2 | Five-fold cross-validation performance (R^2, mean ± standard deviation) for Random Forest (RF) and XGBoost (XGB) models across all feature configurations

Configuration	Model	Young's modulus	Thermal conductivity	Shear modulus	Plastification stress
Full feature set	RF	0.967 ± 0.005	0.978 ± 0.005	0.956 ± 0.010	0.936 ± 0.015
	XGB	0.975 ± 0.007	0.987 ± 0.002	0.968 ± 0.010	0.949 ± 0.019
Excluding V_f	RF	0.944 ± 0.008	0.960 ± 0.013	0.947 ± 0.015	0.929 ± 0.018
	XGB	0.950 ± 0.006	0.972 ± 0.008	0.964 ± 0.011	0.947 ± 0.013
Excluding V_f and I_{11}	RF	0.908 ± 0.031	0.913 ± 0.023	0.923 ± 0.016	0.917 ± 0.023
	XGB	0.926 ± 0.018	0.939 ± 0.015	0.943 ± 0.015	0.931 ± 0.008
Minimal feature set	RF	0.946 ± 0.018	0.959 ± 0.010	0.954 ± 0.009	0.956 ± 0.010
	XGB	0.953 ± 0.017	0.955 ± 0.007	0.958 ± 0.009	0.952 ± 0.011

Geometric features of 3D shapes

An important task for the design of a metamaterial with desired effective performance is to define accurate geometric features.

Volume Fraction: The Volume fraction V_f is defined as the fraction of the material part of Ω with respect to the volume of the unit cell, i.e.:

$$V_f = \frac{|\Omega|}{|\Omega_0|} \tag{5}$$

where $|\Omega| = \int_{\Omega} d\Omega$.

Inner Surface Area: This feature concerns the total normalized area of the inner-architecture that is enclosed in the unit cell Ω_0 and is defined as:

$$A_n = \frac{|\partial\Omega|}{|\partial\Omega_0|} \tag{6}$$

with $|\partial\Omega_0| = 6L^2$ denoting the total area of the unit cell.

Compactness: Compactness is metric that indicates how much is the area of surface compared to the surface of a sphere with equal volumes. Therefore, the definition of Compactness C is given by the following equation:

$$C = \frac{|\partial\Omega|}{|\partial B(\rho^*)|} \tag{7}$$

which an adapted form of the definitions provided in[61]. In Eq. (7), $B(\rho^*)$ is a solid sphere with radius ρ^* such that $|B(\rho^*)| = |\Omega| = \frac{4}{3}\pi\left(\rho^*\right)^3$.

Moments of Inertia: If the unit cell Ω_0 is divided into n x_1x_2 plane sections along the x_3 axis, the moments of inertia with respect to x_1 and x_2 plane directions are obtained by the following averages:

$$\begin{aligned} I_{11} = \tfrac{1}{n}\sum_{k=1}^{n}\widehat{I}_{11}(x_3^k), \quad I_{22} = \tfrac{1}{n}\sum_{k=1}^{n}\widehat{I}_{22}(x_3^k), \quad I_{12} = \tfrac{1}{n}\sum_{k=1}^{n}\widehat{I}_{12}(x_3^k) \\ \widehat{I}_{11}(x_3^k) = \int_{A_k} x_2^2 dA, \quad \widehat{I}_{22}(x_3^k) = \int_{A_k} x_1^2 dA, \quad \widehat{I}_{12}(x_3^k) = \int_{A_k} x_1 x_2 dA \end{aligned} \tag{8}$$

Following the methodology proposed in[53], the unit cell is approximated using a voxelized mesh (Fig. 1d). Thus, the integrals of Eq. (8) are approximated as the following sums:

$$\widehat{I}_{11}(x_3^k) \cong \sum_{i=1}^{n(A_k)} (x_2^i)^2 a_i, \widehat{I}_{22}(x_3^k) \cong \sum_{i=1}^{n(A_k)} (x_1^i)^2 a_i, \widehat{I}_{12}(x_3^k) \cong \sum_{i=1}^{n(A_k)} x_1^i x_2^i a_i \tag{9}$$

where $n(A_k)$ is the number of the voxel faces that are aligned with the A_k cross-section and a_i denotes the voxel face area.

Radial Distance Metrics: Consider a surface $M \subset \mathbb{R}^3$ implicitly defined as the level set:

$$M = \{\mathbf{x} \in \mathbb{R}^3 | F(\mathbf{x}) = c\} \tag{10}$$

where $F : \mathbb{R}^3 \to \mathbb{R}$ is a smooth level set function. In addition, introduce an auxiliary spherical surface $S^2(\rho) = \{\boldsymbol{\xi} \in \mathbb{R}^3 | \parallel \boldsymbol{\xi} \parallel = \rho\}$ where $\boldsymbol{\xi} = (\xi_1, \xi_2, \xi_3)$ and $\rho > 0$. Therefore, the position of $\boldsymbol{\xi}$ can be described using the spherical coordinates:

$$\widehat{\rho}(\boldsymbol{\xi}) = \sqrt{\xi_1^2 + \xi_2^2 + \xi_3^2} \quad \widehat{\theta}(\boldsymbol{\xi}) = \cos^{-1}\frac{\xi_3}{\sqrt{\xi_1^2 + \xi_2^2 + \xi_3^2}} \quad \widehat{\varphi}(\boldsymbol{\xi}) = \cos^{-1}\frac{\xi_1}{\sqrt{\xi_1^2 + \xi_2^2}} \tag{11}$$

For a given point $\boldsymbol{\xi} \in S^2(\rho)$, we seek a point $\mathbf{x} \in M$ lying on the ray emanating from the origin in the direction of $\boldsymbol{\xi}$. This is achieved by solving the nonlinear system:

$$\begin{aligned} R_1(\mathbf{x};\boldsymbol{\xi}) &= F(\mathbf{x}) - c = 0 \\ R_2(\mathbf{x};\boldsymbol{\xi}) &= \cos\widehat{\varphi}(\boldsymbol{\xi}) - \cos\widehat{\varphi}(\mathbf{x}) = c_1(\boldsymbol{\xi})\sqrt{x_1^2 + x_2^2} - x_1 = 0 \\ R_3(\mathbf{x};\boldsymbol{\xi}) &= \cos\widehat{\theta}(\boldsymbol{\xi}) - \cos\widehat{\theta}(\mathbf{x}) = c_2(\boldsymbol{\xi})\sqrt{x_1^2 + x_2^2 + x_3^2} - x_3 = 0 \end{aligned} \tag{12}$$

where $c_1(\boldsymbol{\xi}) = \cos\widehat{\varphi}(\boldsymbol{\xi}) = \frac{\xi_1}{\sqrt{\xi_1^2+\xi_2^2}}$ and $c_2(\boldsymbol{\xi}) = \cos\widehat{\theta}(\boldsymbol{\xi}) = \frac{\xi_3}{\sqrt{\xi_1^2+\xi_2^2+\xi_3^2}}$. For convenience, (12) is written compactly in a vector format as:

$$\mathbf{R}(\mathbf{x};\boldsymbol{\xi}) = \mathbf{0} \tag{13}$$

In the present study, we restrict attention to the positive octant $\xi_1, \xi_2, \xi_3 > 0$, which ensures that the angular coordinates in (11) are well defined and avoids ambiguities arising from symmetry.

For a given $\boldsymbol{\xi}$, the projection f: $\boldsymbol{\xi} \mapsto \mathbf{x}$, is obtained by applying a Newton-Raphson iteration:

$$\begin{aligned} \tfrac{\partial}{\partial \mathbf{x}}\mathbf{R}(\mathbf{x}^{k-1};\boldsymbol{\xi}) \cdot \Delta\mathbf{x} = -\mathbf{R}(\mathbf{x}^{k-1};\boldsymbol{\xi})) \\ \mathbf{x}^k = \mathbf{x}^{k-1} + \Delta\mathbf{x} \end{aligned} \tag{14}$$

starting from an initial guess $\mathbf{x}^0$.

Due to the multiply connected nature of triply periodic minimal surfaces, not all rays admit a well-posed intersection with M. Therefore, only rays for which the Newton procedure converges to a unique intersection point within the prescribed unit cell are retained. Rays leading to no intersection or multiple intersections are discarded. The resulting set is referred to as the set of admissible rays.

Let $G{\circ}S^2(\rho) = \{\boldsymbol{\xi}^i \in S^2, i = 1, 2, \ldots, N_S\}$ denote a discrete sampling of the spherical surface. Solving Eq. (13) for each admissible $\boldsymbol{\xi}^i$ yields a collection of pairs:

$$f(G \circ S^2, G \circ M) = \left\{(\boldsymbol{\xi}, \mathbf{x}) \middle| \boldsymbol{\xi} \in G \circ S^2(\rho), \mathbf{x} \in G \circ M, \mathbf{R}(\mathbf{x};\boldsymbol{\xi}) = \mathbf{0}\right\} \tag{15}$$

With the aid of the collected pairs (15), the following metrics are defined:

$$\begin{aligned} \bar{D} &= \tfrac{1}{N_S}\sum_{i=1}^{N_S} d(\boldsymbol{\xi}^i, \mathbf{x}^i) \\ \mathrm{Var}\,(\mathrm{D}) &= \tfrac{1}{\mathrm{N_S}}\sum_{\mathrm{i}=1}^{\mathrm{N_S}} \left(\mathrm{d}(\boldsymbol{\xi}^{\mathrm{i}}, \mathbf{x}^{\mathrm{i}}) - \widehat{\mathrm{d}}\right)^2 \\ D_{\max} &= \max\left(\left\{d(\boldsymbol{\xi}^i, \mathbf{x}^i)\right\}\right) \\ D_{\min} &= \min\left(\left\{d(\boldsymbol{\xi}^i, \mathbf{x}^i)\right\}\right) \end{aligned} \tag{16}$$

where $d(\boldsymbol{\xi}^i, \mathbf{x}^i) = \|\mathbf{x}^i - \boldsymbol{\xi}^i\|_2$ denotes the Euclidean distance.

In the present work, the surface M corresponds to a triply periodic minimal surface M_{TPMS} defined over a single unit cell of characteristic length L. The radius of the auxiliary spherical surface is chosen as $\rho = 0.5L$ which ensures that ray origins lie within the unit cell and avoids intersections with periodic replicas of the surface. The discrete sampling $G{\circ}S^2(\rho)$ is obtained by a distribution of $N_S = 5810$ Lebedev quadrature points[62].

Machine learning modeling and explainability analysis

Building on the feature definitions and predictive framework introduced in Section 2.3, this section summarizes the training, evaluation, and interpretability pipeline for the Random Forest and Extreme Gradient Boosting models. Both ensemble methods are well suited for nonlinear regression on tabular geometric descriptors and provide strong generalization performance[63,64]. The models are trained using the geometric input vector **X** defined in Eq. (1) to predict the effective properties **Y** defined in Eq. (2). An overview of the Machine Learning Modeling Framework is depicted in Fig. 6.

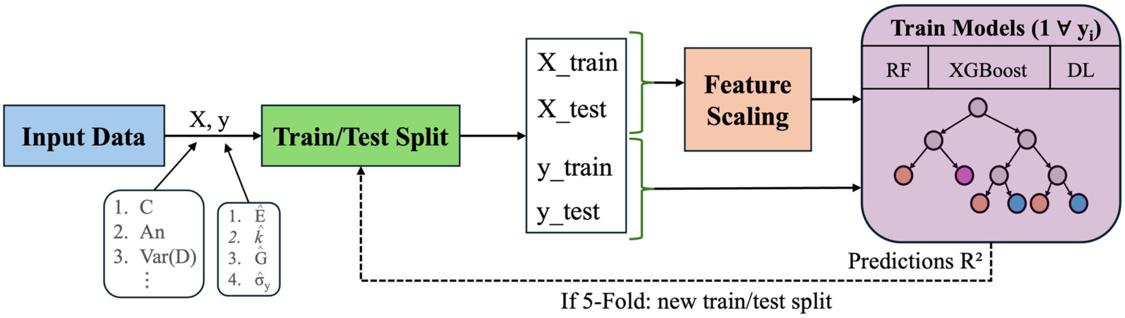

Fig. 6 | Overview of the Machine Learning Modeling Framework. Schematic of the predictive pipeline. Input Data consisting of geometric features and performance targets undergoes Train/Test split. The data is processed through feature scaling before being used to train the models. The framework evaluates predictions using the coefficient of determination and includes an iterative loop for 5-fold cross-validation to ensure model robustness.

Random Forest (RF, `scikit-learn v1.6.1`) and XGBoost regressors (XGB, `xgboost v2.1.4`) were employed, both implemented in Python 3.9.18. Random Forest predictions are obtained as the ensemble average of $n_{\text{trees}} = 100$ decision trees, using the default hyperparameter setting of the associated library.

$$\hat{\mathbf{Y}}_{\text{RF}} = \mathcal{F}_{\text{RF}}(\mathbf{X}) = \frac{1}{n_{\text{trees}}} \sum_{j=1}^{n_{\text{trees}}} \mathcal{F}_j(\mathbf{X}) \tag{17}$$

where $\mathcal{F}_j : \mathbf{X} \mapsto \hat{\mathbf{Y}}$ denotes the jth decision tree. Given the data $\{(\mathbf{X}_i, \mathbf{Y}_i)\}_{i=1}^{N}$, the learning procedure aims seeks the parameters λ^*, such that:

$$\begin{aligned} \boldsymbol{\lambda}^* &= \arg\min_{\boldsymbol{\lambda}} \mathcal{L}(\boldsymbol{\lambda}) \\ \mathcal{L}(\boldsymbol{\lambda}) &= \tfrac{1}{N}\sum_{i=1}^{N} \left(\mathcal{F}_{\text{RF}}(\mathbf{X}_i) - \hat{\mathbf{Y}}_i\right)^2 \end{aligned} \tag{18}$$

XGBoost, in contrast, is a boosting-based ensemble strategy where the prediction of the regressor: $\mathcal{F} : \mathbf{X} \mapsto \hat{\mathbf{Y}}$ is updated iteratively based on a Newton-Raphson procedure:

$$\begin{aligned} \mathcal{F}_m(\mathbf{X}_i) &= \mathcal{F}_{m-1}(\mathbf{X}_i) - \mathcal{H}(\mathbf{X}_i)^{-1}\mathcal{G}(\mathbf{X}_i) \\ \mathcal{G}(\mathbf{X}_i) &= \frac{\partial \mathcal{L}}{\partial \mathcal{F}_{m-1}(\mathbf{X}_i)} = \tfrac{2}{N}\left(\mathcal{F}_{\text{RF}}(\mathbf{X}_i) - \hat{\mathbf{Y}}_i\right) \\ \mathcal{H}(\mathbf{X}_i) &= \frac{\partial^2 \mathcal{L}}{\partial \mathcal{F}_{m-1}(\mathbf{X}_j)\partial \mathcal{F}_{m-1}(\mathbf{X}_i)} = \tfrac{2}{N}\delta_{ji} \end{aligned} \tag{19}$$

where, at each boosting iteration m, the update term $h(\mathbf{X}_i) = \mathcal{H}(\mathbf{X}_i)^{-1}\mathcal{G}(\mathbf{X}_i)$ is fitted to the residual $\mathcal{F}_{\text{RF}}(\mathbf{X}_i) - \hat{\mathbf{Y}}_i$.

All input features were standardized using z-score normalization, where the scaling parameters (mean and standard deviation) were computed on the training subset only and subsequently applied to the test data:

$$\mathbf{X}_i^{(\text{scaled})} = \frac{\mathbf{X}_i - \mu_x}{\sigma_x} \tag{20}$$

The trained machine-learning model, held-out test set, fitted feature standardization object and a standalone evaluation script are publicly available in a Zenodo repository for reproducibility (https://doi.org/10.5281/zenodo.18362271) [65]. Model performance was evaluated on a total of 144 samples, using a stratified 90%/10% train–test split, where stratification was performed with respect to the TPMS topology label, ensuring that each fold contains approximately equal proportions of samples from each TPMS topology. The computing time required for the features estimation and the merely elastic part of the dataset creation ($\widehat{E}$, $\widehat{G}$, $\widehat{\kappa}$) on an AMD Ryzen 9 7950X 16-core processor equipped with a 32 GB RAM was approximately 7.5 hours, corresponding to ~ 188 s per sample. However, for the numerical evaluation of the yield stress limit using the nonlinear elastoplastic FEM analysis, substantially higher computing times were required. In particular, for the yield stress $\widehat{\sigma}_y$ estimations (Section 4.4), approximately 45 minutes (2700 sec) were needed per sample, corresponding to a total of 108 hours for the full set of 144 samples. This leads to an average total time of 2888 s per sample, highlighting the significant computational resources required for the dataset creation. To assess the robustness of the learned structure–property relationships and to identify a reduced yet informative descriptor set, a progressive feature elimination strategy was employed. Four training configurations were considered: (i) the full feature set; (ii) exclusion of the volume fraction V_f; (iii) exclusion of both V_f and the principal moment of inertia I_{11}; and (iv) a minimal feature set comprising only C, A_n, and $Var(D)$, identified through this elimination process.

Predictive accuracy was quantified using the coefficient of determination,

$$R^2 = 1 - \frac{\sum_{i=1}^{N}(\mathbf{Y}_i - \hat{\mathbf{Y}}_i)^2}{\sum_{i=1}^{N}(\mathbf{Y}_i - \bar{Y})^2} \tag{21}$$

Both RF and XGBoost achieve high predictive fidelity across all four target properties and across all training configurations (Fig. 7). Using the full feature set, all models exceed $R^2 = 0.95$, with values reaching up to $R^2 = 0.99$ for thermal conductivity. Importantly, predictive performance remains consistently high under successive feature removal, remaining above $R^2 > 0.92$ even when both V_f and I_{11} are excluded. This confirms that the remaining geometric descriptors retain strong predictive content independent of volumetric and inertial information. Notably, the minimal descriptor set also preserves very high predictive accuracy, with R^2 values exceeding 0.96 across all target properties.

In addition to the train–test evaluation, model robustness was further assessed using 5-fold cross-validation for all feature configurations. This provides a more statistically reliable estimate of model performance by averaging results across multiple folds and reducing the influence of any single data split. Cross-validation performance is reported in terms of the mean and standard deviation of the coefficient of determination across folds (Table 2). Consistent with the hold-out results, both RF and XGBoost exhibit strong and stable predictive performance across all four target properties.

Model interpretability was assessed using both built-in feature importance metrics and SHapley Additive exPlanations (SHAP)[54] computed on the 10% hold-out test set. For a given prediction, the SHAP decomposition is expressed as

$$\hat{Y} = \phi_0 + \sum_{i=1}^{M} \phi_i \tag{22}$$

where ϕ_i denotes the marginal contribution of feature i. The resulting feature rankings and hierarchical geometric interpretation are presented in Section 2.3.

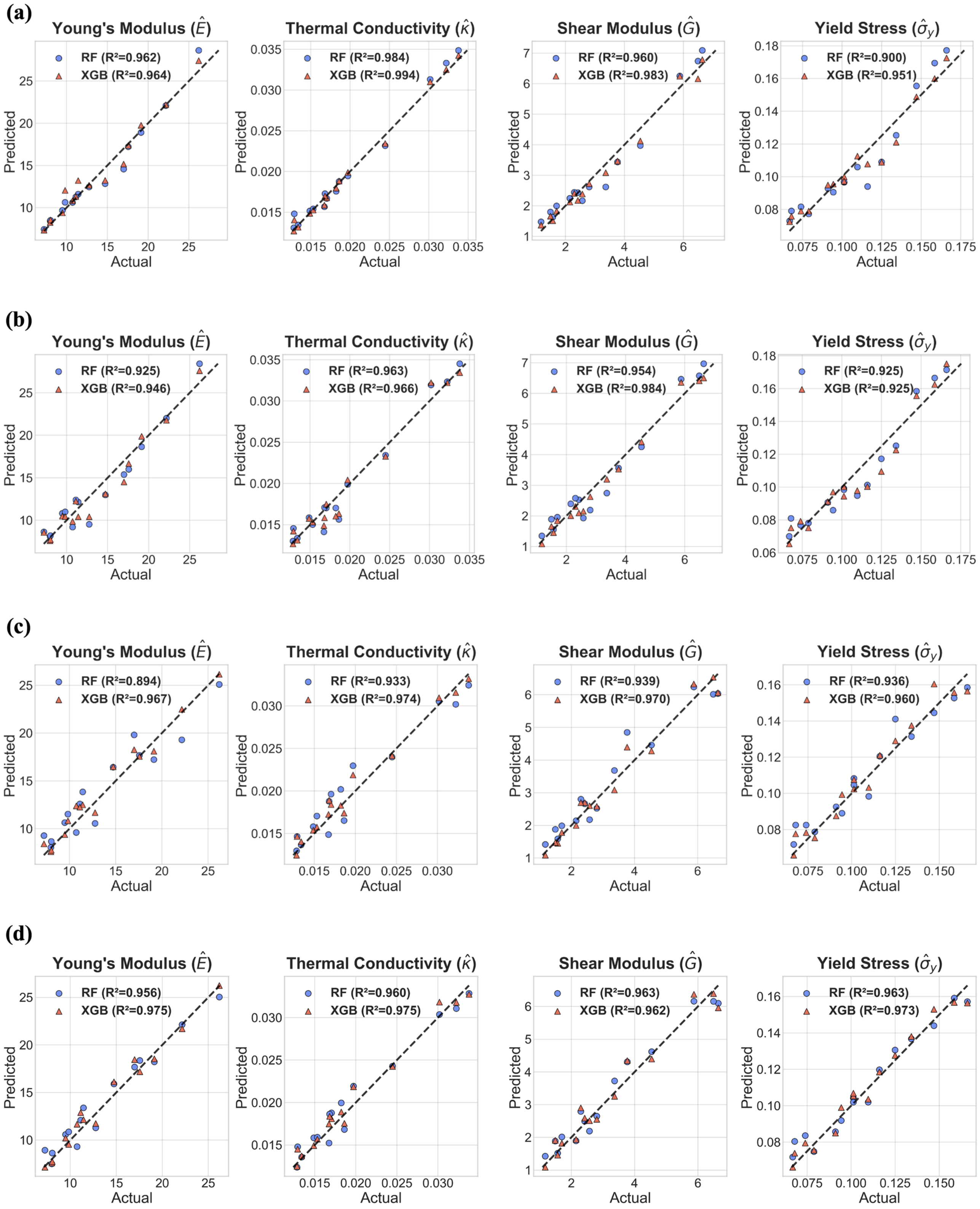

Fig. 7 | Parity plots comparing Random Forest (RF) and XGBoost (XGB) predictions. **a** Full feature set. **b** Excluding volume fraction V_f. **c** Excluding both V_f and I_{11}. **d** Minimum feature set, only using C, A_m, and Var(D). Results are shown for the 10% hold-out test set.

Beyond first-order effects, second-order feature interactions were quantified by computing pairwise correlations between SHAP values of all descriptors. For each target property, the five most influential features were identified based on mean absolute SHAP magnitude. Interaction strength was then evaluated using the absolute Pearson correlation between their SHAP values and those of the remaining features. For each dominant descriptor, the three strongest interaction partners were retained, forming structured interaction maps for all three training configurations. This interaction analysis complements the feature-level hierarchy reported in Section 2.3 and enables systematic assessment of coupled geometric effects.

Table 3 | Level-set equations of selected TPMS and related surfaces

Design	Level-set Equation $\varphi(x_1, x_2, x_3) = t$
GY	$\varphi(x_1, x_2, x_3) : \sin x_1 \cos x_2 + \sin x_2 \cos x_3 + \sin x_3 \cos x_1 = t$
IWP	$\varphi(x_1, x_2, x_3) : 2(\cos x_1 \cos x_2 + \cos x_2 \cos x_3 + \cos x_3 \cos x_1) - (\cos 2x_1 + \cos 2x_2 + \cos 2x_3) = t$
SPC	$\varphi(x_1, x_2, x_3) : \cos x_1 + \cos x_2 + \cos x_3 = t$
FKS	$\varphi(x_1, x_2, x_3) : (\cos x_1 \cos x_2 + \cos x_2 \cos x_3 + \cos x_3 \cos x_1) - (\cos 2x_1 + \cos 2x_2 + \cos 2x_3) = t$
SCD	$\varphi(x_1, x_2, x_3) : \cos x_1 \cos x_2 \cos x_3 - \sin x_1 \sin x_2 \sin x_3 = t$
LD	$\varphi(x_1, x_2, x_3) : \sin 2x_1 \sin x_3 \cos x_2 + \sin 2x_2 \sin x_1 \cos x_3 + \sin 2x_3 \sin x_2 \cos x_1 - \cos 2x_1 \cos 2x_2 + \cos 2x_2 \cos 2x_3 + \cos 2x_3 \cos 2x_1 + 0.3 = t$
SLP	$\varphi(x_1, x_2, x_3) : 1.1 \sin 2x_1 \sin x_3 \cos x_2 + \sin 2x_2 \sin x_1 \cos x_3 + \sin 2x_3 \sin x_2 \cos x_1 - 0.2 \cos 2x_1 \cos 2x_2 + \cos 2x_2 \cos 2x_3 + \cos 2x_3 \cos 2x_1 - 0.4 \cos x_1 + \cos x_2 + \cos x_3 = t$
I2Y	$\varphi(x_1, x_2, x_3) : -2 \sin 2x_1 \cos x_2 \sin x_3 + \sin x_1 \sin 2x_2 \cos x_3 + \cos x_1 \sin x_2 \sin 2z + \cos 2x_1 \cos 2x_2 + \cos 2x_2 \cos 2x_3 + \cos 2x_1 \cos 2x_3 = t$
FRD	$\varphi(x_1, x_2, x_3) : 4 \cos x_1 \cos x_2 \cos x_3 - (\cos 2x_1 \cos 2x_2 + \cos 2x_2 \cos 2x_3 + \cos 2x_3 \cos 2x_1) = t$

Data generation through voxel finite element method

Assuming infinitesimal strains and a homogeneous, isotropic material in the domain Ω, and neglecting both distributed elastic and thermal body loads, the steady-state displacement and temperature fields $\mathbf{u}: \mathbf{x} \mapsto (u_1(\mathbf{x}), u_2(\mathbf{x}), u_3(\mathbf{x}))$ and $\theta: \mathbf{x} \mapsto \theta(\mathbf{x})$ satisfy the following system of partial differential equations:

$$\begin{array}{c} \nabla \cdot \tilde{\boldsymbol{\sigma}}(\mathbf{u}) = \mathbf{0}, \nabla \cdot \mathbf{q}(\theta) = 0 \\ \tilde{\boldsymbol{\sigma}}(\mathbf{u}) = f(\tilde{\epsilon}(\mathbf{u})), \tilde{\boldsymbol{\epsilon}}(\mathbf{u}) = \frac{1}{2}(\nabla\mathbf{u} + \mathbf{u}\nabla), \mathbf{q}(\theta) = -\kappa\nabla\theta \end{array}, \mathbf{x} \in \Omega_0 \tag{23}$$

where $\tilde{\boldsymbol{\sigma}}(\mathbf{u}) = \tilde{\sigma}_{ij}(\mathbf{u})\hat{\mathbf{x}}_i \otimes \hat{\mathbf{x}}_j$, $\tilde{\boldsymbol{\epsilon}}(\mathbf{u}) = \tilde{e}_{ij}(\mathbf{u})\hat{\mathbf{x}}_i \otimes \hat{\mathbf{x}}_j$ and $\mathbf{q}(\theta) = q_i(\theta)\hat{\mathbf{x}}_i$ denote the stress and strain second-rank tensors and heat flux vector, respectively. The mechanical and thermal boundary value problems are complemented employing uniform displacement and temperature periodic boundary conditions[25,66] on the boundary Γ_D. For the linear elastic case, the mechanical constitutive law of Eq. (23), that relates the stress with the strain tensor, reduces to Hooke's law: $\tilde{\boldsymbol{\sigma}}(\mathbf{u}) = \lambda(\nabla \cdot \mathbf{u})\tilde{\mathbf{I}} + \mu(\nabla\mathbf{u} + \mathbf{u}\nabla)$, where the Lame parameters $\lambda = \lambda(E, \nu)$ and $\mu = \mu(E, \nu)$ are functions of the phase material Young's modulus E and Poisson's ratio ν [25].

Considering the functional spaces $V_w = \left\{\mathbf{w} \in [H^1(\Omega_0)]^3 \middle| \ \mathbf{w} = \mathbf{0} \text{ on } \Gamma_D\right\}$ and $V_\upsilon = \{\upsilon \in H^1(\Omega_0) | \upsilon = 0 \text{ on } \Gamma_D\}$, the following weak forms are obtained by multiplying the first-row equations of Eq. (23) with $\mathbf{w} \in V_w$ and $\upsilon \in V_\upsilon$, respectively, and integrating on Ω_0[67]:

$$\begin{array}{r} \text{Find } \mathbf{u} \in V_u \text{ such that } : \int_{\partial\Omega_0} \mathbf{w} \cdot [\mathbf{n} \cdot \tilde{\boldsymbol{\sigma}}(\mathbf{u})] d\Gamma - \int_{\Omega_0} \nabla\mathbf{w} : \tilde{\boldsymbol{\sigma}}(\mathbf{u}) d\Omega = 0, \forall \mathbf{w} \in V_w \\ \text{Find } \theta \in V_\theta \text{ such that } : \int_{\partial\Omega_0} \upsilon[\kappa\mathbf{n} \cdot \nabla\theta] d\Gamma - \int_{\Omega_0} \kappa\nabla\upsilon \cdot \nabla\theta d\Omega = 0, \forall \upsilon \in V_\upsilon \end{array} \tag{24}$$

where $V_u = \left\{\mathbf{u} \in [H^1(\Omega_0)]^3 | \mathbf{u} = \mathbf{u}_0 \text{ on } \Gamma_D\right\}$ and $V_\theta = \{\theta \in H^1(\Omega_0) | \theta = \theta_0 \text{ on } \Gamma_D\}$.

The unit cell Ω_0 is discretized into a set of N_{Ω_0} 8-noded brick elements K (voxels), defined as $\mathcal{T}(\Omega_0) = \bigcup_{j=1}^{N_{\Omega_0}} K_j$. The set of voxels belonging to the material phase is defined as $\mathcal{T}(\Omega) = \{K \in \mathcal{T}(\Omega_0) | K \cap \Omega = \}$. Assuming linear elasticity, the weak forms of Eq. (24) lead to finite element formulations, therefore, the displacement $\mathbf{u}$ and temperature values θ are obtained on the nodes of the voxel mesh $\mathcal{T}(\Omega_0)$. Commercial Ansys APDL and voxel-finite element analysis comparisons are provided in Figure S1 of the Supplementary Material, along with detailed convergence analysis results, and extended literature comparisons on the effective performance. The obtained nodal values, are employed to calculate the effective material properties based to the following relations[25,66]:

$$\widehat{E} = \frac{\langle\sigma_{11}\rangle|_{\Omega_0}}{\epsilon_0} \quad \widehat{G} = \frac{\langle\sigma_{12}\rangle|_{\Omega_0}}{\gamma_0} \quad \widehat{\kappa} = \frac{\langle q_1\rangle|_{\Omega_0}}{q_0} \tag{25}$$

where $\langle\sigma_{11}\rangle|_{\Omega_0}$, $\langle\sigma_{12}\rangle|_{\Omega_0}$, $\langle q_1\rangle|_{\Omega_0}$ denote the average components of the stress tensor and heat flux vector, with $\langle f\rangle|_{\Omega_0} = \frac{1}{|\Omega_0|}\int_{\Omega_0} f d\Omega$ representing the average of a function f. It should be noted that a value of 27000 for the N_{Ω_0} appears to be sufficient for convergent results on the above performance metrics, as summarized in the Supplementary Material (S1).

The effective elastoplastic response of the unit cell Ω_0 is modeled, based on the J_2 plasticity with isotropic hardening[67]. For a bilinear material law, the plastified stress tensor $\tilde{\boldsymbol{\sigma}}$ should satisfy the yield surface, described by the following level set equation:

$$f(\tilde{\boldsymbol{\sigma}}, \kappa) = \| \tilde{\boldsymbol{\sigma}} \|_{VM} - (\sigma_{y,0} + H\dot{\epsilon}_p) = 0 \tag{26}$$

where $\| \tilde{\boldsymbol{\sigma}} \|_{VM} = \sqrt{\frac{3}{2}\tilde{\mathbf{s}} : \tilde{\mathbf{s}}}$ denotes the von Mises equivalent stress, with $\tilde{\mathbf{s}}$ being the deviator of $\tilde{\boldsymbol{\sigma}}$, while $\sigma_{y,0}$, H and $\mathring{\epsilon}_p$ are the base material yield limit, the hardening rate and the accumulated plastic strain, respectively. Based on the yield criterion, the material plastification is characterized by the following binary indicator:

$$P(\mathbf{x}) = \begin{cases} 1, f(\tilde{\boldsymbol{\sigma}}(\mathbf{x}), \kappa(\mathbf{x})) = 0 \\ 0, f(\tilde{\boldsymbol{\sigma}}(\mathbf{x}), \kappa(\mathbf{x})) < 0 \end{cases} \tag{27}$$

which distinguishes plastified and elastic regions within the unit cell. This definition leads to the set of plastified voxels:

$$\mathcal{P}(\Omega_0) = \{K \in \mathcal{T}(\Omega_0) | P(\hat{\mathbf{x}}_K) = 1\} \tag{28}$$

where $\hat{\mathbf{x}}_K$ is the centroid of the voxel K. In the sequel, the plastification volume fraction V_p is defined as:

$$V_p = \frac{1}{|\Omega_0|}\int_{\Omega_0} P(\mathbf{x}) d\Omega \cong \frac{1}{|\Omega_0|}\sum_{K \in \mathcal{P}(\Omega_0)} |K| \tag{29}$$

Therefore, the effective yield stress is defined as the average von-Mises stress in order to achieve $V_p = 0.1\%$.

$$\widehat{\sigma}_y = \frac{\langle \| \tilde{\boldsymbol{\sigma}} \|_{VM} \rangle|_{\Omega_0}}{\sigma_{y,0}} \tag{30}$$

The threshold value of $V_p = 0.1\%$ is chosen sufficiently small to characterize the initiation of plastic deformation. In the present study, the base material is considered to be aluminium with an initial yield limit $\sigma_{y,0} = 250$MPa and an assumed hardening rate $H = 0.1 \times E = 6.9$ GPa.

It should be noted that the use of Voxel-FEM methods for the mechanical analysis of such a large number of TPMS structures is to a great extent dictated by the limitations of current CAD TPMS modeling and mechanical analysis programs. These are not directly linked, so that the post-processing steps required for the translation of a mere CAD TPMS model, typically provided in an .stl file, thus surface type formatting to a solid FEM model that can be properly meshed and analyzed in standard Finite element analysis software packages are particularly labor, and computational resources intensive. In particular, the intermediate surface to volume conversion steps are not automated, requiring substantial computational resources and excessive working times for the processing of hundreds of models. These intermediate conversion steps are decisively simplified in the Voxel-FEM formulation, as the CAD geometry is directly converted to a solid voxel mesh through the use of the implicit field φ function of Table 3 for each topology, which is used as a domain identification equation, separating solid voxels from the surrounding empty material space. As such, parametric, sufficient sample dataset creation tasks are particularly facilitated.

Data availability

The data required to reproduce and interpret the primal findings of this work are provided in the following Zenodo Repository: https://doi.org/10.5281/zenodo.18362271.

Code availability

The code required to reproduce the primal findings of this work is provided in the following Zenodo Repository.

Received: 24 December 2025; Accepted: 21 February 2026;

References

1. Zadpoor, A. A. Mechanical meta-materials. *Mater. Horiz.* **3**, 371–381 (2016).
2. Fan, J. et al. A review of additive manufacturing of metamaterials and developing trends. *Mater. Today* **50**, 303–328 (2021).
3. Kulagin, R. et al. Lattice metamaterials with mesoscale motifs: exploration of property charts by bayesian optimization. *Adv. Eng. Mater.* **25**, 2300048 (2023).
4. Zhang, M. et al. Breaking stiffness-tunability trade-offs in metamaterials: a minimal surface guided hybrid lattice strategy. *Adv. Sci.* **12**, e10586 (2025).
5. Yu, X., Zhou, J., Liang, H., Jiang, Z. & Wu, L. Mechanical metamaterials associated with stiffness, rigidity and compressibility: a brief review. *Prog. Mater. Sci.* **94**, 114–173 (2018).
6. Akhmetshin, L., Iokhim, K., Kazantseva, E. & Smolin, I. Influence of topological defects on the mechanical response of unit cells of the tetrachiral mechanical metamaterial. *Designs* **7**, 129 (2023).
7. Jaber, A., Singh, A., Rodopoulos, D. C. & Karathanasopoulos, N. Inner design and strain-rate effects on the performance of architected materials and interpenetrating phase composites: state-of-the-art analysis and perspectives. *Adv. Eng. Mater.* **27**, 2500870 (2025).
8. Sharma, S. et al. Piezoelectric truss metamaterials: data-driven design and additive manufacturing. *npj Metamaterials* **1**, 9 (2025).
9. Bertoldi, K. Harnessing instabilities to design tunable architected cellular materials. *Annu. Rev. Mater. Res.* **47**, 51–61 (2017).
10. He, R., Chen, Y., Shi, J., Bai, Y. & Feng, J. Programming morphological and mechanical performance of cyclic ori-kirigami via design-feasible parameter space. *Thin-Walled Struct.* **207**, 112706 (2025).
11. Surjadi, J. U. et al. Mechanical metamaterials and their engineering applications. *Adv. Eng. Mater.* **21**, 1800864 (2019).
12. Liu, H., Falzon, B. G. & Tan, W. Experimental and numerical studies on the impact response of damage-tolerant hybrid unidirectional/woven carbon-fibre reinforced composite laminates. *Compos. Part B Eng.* **136**, 101 (2018).
13. Janbaz, S., Narooei, K., van Manen, T. & Zadpoor, A. A. Strain rate-dependent mechanical metamaterials. *Sci. Adv.* **6**, eaba0616 (2020).
14. Surjadi, J. U., Aymon, B. F. G., Carton, M. & Portela, C. M. Double-network-inspired mechanical metamaterials. *Nat. Mater.* **24**, 945–954 (2025).
15. Li, Z. et al. Unprecedented mechanical wave energy absorption observed in multifunctional bioinspired architected metamaterials. *NPG Asia Mater*. **16** (2024).
16. Thakolkaran, P., Espinal, M., Dhulipala, S., Kumar, S. & Portela, C. M. Experiment-informed finite-strain inverse design of spinodal metamaterials. *Extrem. Mech. Lett.* **74**, 102274 (2025).
17. Xiao, L. et al. Mechanical characterization of additively-manufactured metallic lattice structures with hollow struts under static and dynamic loadings. *Int. J. Impact Eng.* **169**, 104333 (2022).
18. Al-Ketan, O., Rowshan, R. & Abu Al-Rub, R. K. Topology-mechanical property relationship of 3d printed strut, skeletal, and sheet based periodic metallic cellular materials. *Addit. Manuf.* **19**, 167–183 (2018).
19. Karathanasopoulos, N. & Rodopoulos, D. C. Enhanced cellular materials through multiscale, variable-section inner designs: Mechanical attributes and neural network modeling. *Materials* **15** (2022).
20. Karathanasopoulos, N. & Al-Ketan, O. Towards biomimetic, lattice-based, tendon and ligament metamaterial designs. *J. Mech. Behav. Biomed. Mater.* **134**, 105412 (2022).
21. Gu, G. X., Takaffoli, M. & Buehler, M. J. Hierarchically enhanced impact resistance of bioinspired composites. *Adv. Mater.* **29**, 1700060 (2017).
22. Karathanasopoulos, N. & Dos Reis, F. Extending the elastic and plastic design space of metamaterials through load-specific, multiscale inner material architectures. *Int. J. Mech. Sci.* **175**, 105523 (2020).
23. de Jonge, C. P., Kolken, H. M. A. & Zadpoor, A. A. Non-auxetic mechanical metamaterials. *Materials* **12**, 635 (2019).
24. Kulagin, R., Beygelzimer, Y., Estrin, Y., Schumilin, A. & Gumbsch, P. Architectured lattice materials with tunable anisotropy: Design and analysis of the material property space with the aid of machine learning. *Adv. Eng. Mater.* **22**, 2001069 (2020).
25. Rodopoulos, D. C. & Karathanasopoulos, N. Thermomechanical performance of double-phase periodic and graded architected materials: Numerical and explainability analysis. *Int. J. Solids Struct.* **309**, 113159 (2025).
26. Andersson, S., Hyde, S., Larsson, K. & Lidin, S. Minimal surfaces and structures: from inorganic and metal crystals to cell membranes and biopolymers. *Chem. Rev.* **88**, 221–242 (1988).
27. Al-Ketan, O. & Al-Rub, R. K. A. Multifunctional mechanical metamaterials based on triply periodic minimal surface lattices. *Adv. Eng. Mater.* **21**, 1900524 (2019).
28. Singh, A. & Karathanasopoulos, N. Strut and stochastic polymer reinforcement interpenetrating phase composites: Static, strain-rate and dynamic damping performance. *Thin-Walled Struct.* **198**, 111618 (2024).
29. Singh, A., Al-Ketan, O. & Karathanasopoulos, N. Highly strain-rate sensitive and ductile composite materials combining soft with stiff tpms polymer-based interpenetrating phases. *Composite Struct.* **328**, 117646 (2024).
30. Zhao, X., Li, Z., Zou, Y. & Zhao, X. Compressive characteristics and energy absorption capacity of automobile energy-absorbing box with filled porous tpms structures. *Appl. Sci*. **14** (2024).
31. Xiao, L. et al. Large deformation response of a novel triply periodic minimal surface skeletal-based lattice metamaterial with high stiffness and energy absorption. *Int. J. Solids Struct.* **296**, 112830 (2024).

32. Baobaid, N., Ali, M. I., Khan, K. A. & Abu Al-Rub, R. K. Fluid flow and heat transfer of porous tpms architected heat sinks in free convection environment. *Case Stud. Therm. Eng.* **33**, 101944 (2022).
33. Mueller, J., Lewis, J. A. & Bertoldi, K. Architected multimaterial lattices with thermally programmable mechanical response. *Adv. Funct. Mater.* **32**, 2105128 (2022).
34. Schoen, A. H. Infinite periodic minimal surfaces without self-intersections. NASA Technical Note NASA TN D-5541, (NASA Electronics Research Center, 1970).
35. Corkery, R. W. & Tyrode, E. C. On the colour of wing scales in butterflies: iridescence and preferred orientation of single gyroid photonic crystals. *Interface Focus* **7**, 20160154 (2017).
36. Zhang, L. et al. Energy absorption characteristics of metallic triply periodic minimal surface sheet structures under compressive loading. *Addit. Manuf.* **23**, 505–515 (2018).
37. Naghavi, S. A. et al. Mechanical characterisation and numerical modelling of TPMS-based gyroid and diamond Ti6Al4V scaffolds for bone implants: An integrated approach for translational consideration. *Bioengineering* **9**, 504 (2022).
38. Jaber, A., Singh, A., Rodopoulos, D. C. & Karathanasopoulos, N. Hybrid manufacturing and mechanics of copper-based architected materials and copper-aluminum interpenetrating phase composites. *J. Mater. Res. Technol.* **38**, 674–691 (2025).
39. Xia, L. & Breitkopf, P. Multiscale structural topology optimization with an approximate constitutive model for local material microstructure. *Computer Methods Appl. Mech. Eng.* **286**, 147–167 (2015).
40. Wang, C. et al. Concurrent design of hierarchical structures with three-dimensional parameterized lattice microstructures for additive manufacturing. *Struct. Multidiscip. Optim.* **61**, 869–894 (2020).
41. Kumar, T., Sridhara, S., Prabhune, B. & Suresh, K. Spectral decomposition for graded multi-scale topology optimization. *Computer Methods Appl. Mech. Eng.* **377**, 113670 (2021).
42. Zhao, M. et al. Machine learning accelerated design of lattice metamaterials for customizable energy absorption. *Thin-Walled Struct.* **208**, 112845 (2025).
43. Dos Reis, F. & Karathanasopoulos, N. Deep learning, deconvolutional neural network inverse design of strut-based lattice metamaterials. *Comput. Mater. Sci.* **244**, 113258 (2024).
44. Yang, C., Kim, Y., Ryu, S. & Gu, G. X. Using convolutional neural networks to predict composite properties beyond the elastic limit. *MRS Commun.* **9**, 609–617 (2019).
45. Rong, Q., Wei, H., Huang, X. & Bao, H. Predicting the effective thermal conductivity of composites from cross sections images using deep learning methods. *Compos. Sci. Technol.* **184**, 107861 (2019).
46. Rodopoulos, D. C., Pantidis, P. & Karathanasopoulos, N. Variational pinns with tree-based integration and boundary element data in the modeling of multi-phase architected materials. *Eng. Anal. Bound. Elem.* **180**, 106448 (2025).
47. Meyer, P. P., Bonatti, C., Tancogne-Dejean, T. & Mohr, D. Graph-based metamaterials: Deep learning of structure-property relations. *Mater. Des.* **223**, 111175 (2022).
48. Zheng, X., Chen, T.-T., Guo, X., Samitsu, S. & Watanabe, I. Controllable inverse design of auxetic metamaterials using deep learning. *Mater. Des.* **211**, 110178 (2021).
49. Putin, E. et al. Adversarial threshold neural computer for molecular de Novo design. *Mol. Pharm.* **15**, 4386–4397 (2018).
50. Challapalli, A., Patel, D. & Li, G. Inverse machine learning framework for optimizing lightweight metamaterials. *Mater. Des.* **208**, 109937 (2021).
51. He, J., Kushwaha, S., Abueidda, D. & Jasiuk, I. Exploring the structure-property relations of thin-walled, 2D extruded lattices using neural networks. *Comput. Struct.* **277-278**, 106940 (2023).
52. Qian, C., Kaminer, I. & Chen, H. A guidance to intelligent metamaterials and metamaterials intelligence. *Nat. Commun.* **16**, 1154 (2025).
53. Hassan, I. U. et al. Tuning structural dynamics through architected inner material designs: Numerical, experimental, and machine learning analysis. *Mater. Des.* **256**, 114184 (2025).
54. Lundberg, S. M. & Lee, S.-I. A unified approach to interpreting model predictions. In *Advances in Neural Information Processing Systems*, 4765–4774 (2017).
55. Koptelov, A., Beketova, H., Belnoue, J. P.-H., Hallett, S. R. & Tretiak, I. Addressing data scarcity in deep learning: Leveraging real and artificial datasets to predict compaction of composites. *Mater. Des.* **257**, 114536 (2025).
56. Hakami, A. Strategies for overcoming data scarcity, imbalance, and feature selection challenges in machine learning models for predictive maintenance. *Sci. Rep.* **14**, 9645 (2024).
57. Jo, T.*Machine Learning Foundations: Supervised, Unsupervised, and Advanced Learning* (Springer, Cham, Switzerland, 2021). Includes supervised, unsupervised, and advanced machine learning algorithms.
58. Freschlin, C. R., Fahlberg, S. A., Heinzelman, P. & Romero, P. A. Neural network extrapolation to distant regions of the protein fitness landscape. *Nat. Commun.* **15**, 6405 (2024).
59. Altamimi, S. et al. Stiffness, strength, anisotropy, and buckling of lattices derived from tpms and platonic and archimedean solids. *Mech. Adv. Mater. Struct.* **32**, 79–106 (2025).
60. Singh, A., Al-Ketan, O. & Karathanasopoulos, N. Mechanical performance of solid and sheet network-based stochastic interpenetrating phase composite materials. *Compos. Part B Eng.* **251**, 110478 (2023).
61. Bribiesca, E. An easy measure of compactness for 2d and 3d shapes. *Pattern Recognit.* **41**, 543–554 (2008).
62. Lebedev, V. Quadratures on a sphere. *USSR Comput. Math. Math. Phys.* **16**, 10–24 (1976).
63. Breiman, L. Random forests. *Machine Learning* **45**, 5–32 (2001).
64. Chen, T. & Guestrin, C. Xgboost: A scalable tree boosting system. In *Proceedings of the 22nd ACM SIGKDD International Conference on Knowledge Discovery and Data Mining*, 785–794 (2016).
65. Rodopoulos, D., Mermigkis, G., Hadjidoukas, P. & Karathanasopoulos, N. Machine learning based mechanics of tpms architected materials driven by unit-cell geometric features (reproducibility software) (2026).
66. Kanit, T., Forest, S., Galliet, I., Mounoury, V. & Jeulin, D. Determination of the size of the representative volume element for random composites: statistical and numerical approach. *Int. J. Solids Struct.* **40**, 3647–3679 (2003).
67. Simo, J. C. & Hughes, T. J. R.*Computational Inelasticity* (Springer New York, 2006).

Acknowledgements

The authors gratefully acknowledge the support of the computational resources of the High Performance Computing Center at New York University Abu Dhabi. Additionally, the authors thank the Computer Centre of the Department of Computer Engineering & Informatics at the University of Patras for providing essential computing infrastructure supporting this research. N.K. would like to gratefully acknowledge the support of the Starting Grant of NYU AD.

Author contributions

D.R. and G.M. worked on diverse aspects, including computational analysis, machine learning, and figure preparation. P.H. worked on diverse computational aspects, including feature generation together with N.K., who conceptualized this research. N.K and P.H. supervised the research. N.K, D.R., and G.M. wrote the initial draft, and all authors contributed to editing and revising the manuscript.

Competing interests

The authors declare no competing interests.

Additional information

Supplementary information The online version contains supplementary material available at https://doi.org/10.1038/s44455-026-00026-9.

Correspondence and requests for materials should be addressed to Nikolaos Karathanasopoulos.

Reprints and permissions information is available at http://www.nature.com/reprints

Publisher's note Springer Nature remains neutral with regard to jurisdictional claims in published maps and institutional affiliations.

Open Access This article is licensed under a Creative Commons Attribution-NonCommercial-NoDerivatives 4.0 International License, which permits any non-commercial use, sharing, distribution and reproduction in any medium or format, as long as you give appropriate credit to the original author(s) and the source, provide a link to the Creative Commons licence, and indicate if you modified the licensed material. You do not have permission under this licence to share adapted material derived from this article or parts of it. The images or other third party material in this article are included in the article's Creative Commons licence, unless indicated otherwise in a credit line to the material. If material is not included in the article's Creative Commons licence and your intended use is not permitted by statutory regulation or exceeds the permitted use, you will need to obtain permission directly from the copyright holder. To view a copy of this licence, visit http://creativecommons.org/licenses/by-nc-nd/4.0/.

© The Author(s) 2026